2022-12

FAILURE OF BOLT FASTENED BRITTLE MATERIALS

Gonzalez, Adrian A.

Monterey, CA; Naval Postgraduate School

NAVAL POSTGRADUATE SCHOOL

MONTEREY, CALIFORNIA

THESIS

FAILURE OF BOLT FASTENED BRITTLE MATERIALS

by

Adrian A. Gonzalez

December 2022

Thesis Advisor: Young W. Kwon
Second Reader: Jarema M. Didoszak

THIS PAGE INTENTIONALLY LEFT BLANK

REPORT DOCUMENTATION PAGE	*Form Approved OMB No. 0704-0188*

1. AGENCY USE ONLY *(Leave blank)*	**2. REPORT DATE** December 2022	**3. REPORT TYPE AND DATES COVERED** Master's thesis

4. TITLE AND SUBTITLE
FAILURE OF BOLT FASTENED BRITTLE MATERIALS

5. FUNDING NUMBERS

6. AUTHOR(S) Adrian A. Gonzalez

7. PERFORMING ORGANIZATION NAME(S) AND ADDRESS(ES)
Naval Postgraduate School
Monterey, CA 93943-5000

8. PERFORMING ORGANIZATION REPORT NUMBER

9. SPONSORING / MONITORING AGENCY NAME(S) AND ADDRESS(ES)
N/A

10. SPONSORING / MONITORING AGENCY REPORT NUMBER

11. SUPPLEMENTARY NOTES The views expressed in this thesis are those of the author and do not reflect the official policy or position of the Department of Defense or the U.S. Government.

12a. DISTRIBUTION / AVAILABILITY STATEMENT
Approved for public release. Distribution is unlimited.

12b. DISTRIBUTION CODE
A

13. ABSTRACT (maximum 200 words)

Since the early twentieth century, a substantial number of models, theories, and computational methods have been developed to predict material failure in brittle and quasi-brittle materials. In most cases, the proposed models and theories can only predict failure under very specific conditions. A unified failure criteria has recently been proposed to eliminate the need for multiple failure criteria, and early work has shown promising results for brittle and quasi-brittle materials under uniaxial tensile loading. This thesis aimed to further validate the proposed failure criteria using a more complex and common loading/failure condition, namely, bolt fastened material failure. The failure of bolt fastened poly(methyl methacrylate) (PMMA) and carbon fiber composites (CFC) was assessed using the newly proposed criteria. Inaccuracies in the failure predictions of bolt fastened brittle materials resulted in the discovery of new information. Results from experimental and numerical data strongly suggests that, for a brittle isotropic material, the location of failure initiation and the direction of initial crack propagation coincides with the maximum principal stress and the plane perpendicular to the maximum principal stress vector.

14. SUBJECT TERMS
poly(methyl methacrylate), PMMA, carbon fiber composite, CFC, carbon fiber, bolt fastened, bolted joint, modes of failure, failure, material failure

15. NUMBER OF PAGES
99

16. PRICE CODE

17. SECURITY CLASSIFICATION OF REPORT	**18. SECURITY CLASSIFICATION OF THIS PAGE**	**19. SECURITY CLASSIFICATION OF ABSTRACT**	**20. LIMITATION OF ABSTRACT**
Unclassified	Unclassified	Unclassified	UU

NSN 7540-01-280-5500

Standard Form 298 (Rev. 2-89)
Prescribed by ANSI Std. 239-18

THIS PAGE INTENTIONALLY LEFT BLANK

Approved for public release. Distribution is unlimited.

FAILURE OF BOLT FASTENED BRITTLE MATERIALS

Adrian A. Gonzalez
Lieutenant, United States Navy
BS, University of Nevada, Las Vegas, 2015

Submitted in partial fulfillment of the
requirements for the degree of

MASTER OF SCIENCE IN MECHANICAL ENGINEERING

from the

NAVAL POSTGRADUATE SCHOOL
December 2022

Approved by: Young W. Kwon
Advisor

Jarema M. Didoszak
Second Reader

Brian S. Bingham
Chair, Department of Mechanical and Aerospace Engineering

THIS PAGE INTENTIONALLY LEFT BLANK

ABSTRACT

Since the early twentieth century, a substantial number of models, theories, and computational methods have been developed to predict material failure in brittle and quasi-brittle materials. In most cases, the proposed models and theories can only predict failure under very specific conditions. A unified failure criteria has recently been proposed to eliminate the need for multiple failure criteria, and early work has shown promising results for brittle and quasi-brittle materials under uniaxial tensile loading. This thesis aimed to further validate the proposed failure criteria using a more complex and common loading/failure condition, namely, bolt fastened material failure. The failure of bolt fastened poly(methyl methacrylate) (PMMA) and carbon fiber composites (CFC) was assessed using the newly proposed criteria. Inaccuracies in the failure predictions of bolt fastened brittle materials resulted in the discovery of new information. Results from experimental and numerical data strongly suggests that, for a brittle isotropic material, the location of failure initiation and the direction of initial crack propagation coincides with the maximum principal stress and the plane perpendicular to the maximum principal stress vector.

THIS PAGE INTENTIONALLY LEFT BLANK

TABLE OF CONTENTS

LIST OF FIGURES

LIST OF TABLES

THIS PAGE INTENTIONALLY LEFT BLANK

LIST OF ACRONYMS AND ABBREVIATIONS

ACP	Ansys Composite PrepPost
C1	cross-ply part 1
C2	cross-ply part 2
CAD	computer-aided design
CFC	carbon fiber composite
CP	cross-ply
FEA	finite element analysis
FFM	finite fracture mechanics
LEFM	linear elastic fracture mechanics
NPS	Naval Postgraduate School
P1	poly(methyl methacrylate) part 1
P2	poly(methyl methacrylate) part 2
P3	poly(methyl methacrylate) part 3
P4	poly(methyl methacrylate) part 4
P5	poly(methyl methacrylate) part 5
P6	poly(methyl methacrylate) part 6
PMMA	poly(methyl methacrylate)
Q1	quasi-isotropic part 1
Q2	quasi-isotropic part 2
QI	quasi-isotropic
SCF	stress concentration factor
SEM	scanning electron microscope
SIF	stress intensity factor
TCD	theory of critical distances

THIS PAGE INTENTIONALLY LEFT BLANK

ACKNOWLEDGMENTS

First and foremost, I would like to thank my beautiful wife, Jenna, and my amazing children, Jacob, Saylor, Grey, and Indie. They have had to sacrifice a significant amount of time away from me during this endeavor. Their love and support have and will continue to be the root of my success. I would also like to thank my father and grandparents for their unconditional love and support. My grandfather, Dennis Fiske, has been involved in many of my school projects and this thesis was no different. Thank you for all your help, Grandpa.

Lastly, I would like to thank all the professors that I have had while attending the Naval Postgraduate School. Each and every professor, which I have been fortunate to have, has contributed to my success. I would especially like to thank Professor Kwon, my thesis advisor. He has been inspirational and has provided invaluable guidance throughout my time here.

THIS PAGE INTENTIONALLY LEFT BLANK

I. INTRODUCTION

A significant amount of time and money are spent ensuring newly designed physical products do not fail while performing their intended use. In addition to inadequate performance, an improperly designed product may potentially result in additional cost, time, injury, or worst case, loss of life [1], [2]. Critical to every successfully designed product is proper material selection [2]–[4]. More specifically, a material must be selected that will not fail under expected loading conditions.

Over the years, a considerable number of theories, models, and criteria have been proposed to predict material failure [1], [3], [4]. Unfortunately, the degree of accuracy amongst the various theories and models has been shown to differ as the material conditions have been altered. Changes to the materials loading conditions, structural constraints, or geometry have all been shown to have an effect on the present models. Therefore, numerous models continue to be utilized, and model selection is based on the accuracy of predictions for a given set of conditions. Fortunately, a newly proposed set of failure criteria has shown early signs of reducing the number of models currently in use for predicting brittle fracture.

Motivated to create a singular set of failure criteria, Y. W. Kwon has recently proposed a set of failure criteria that has shown promising results for brittle materials [5], [6]. Thus far, Kwon's work has accurately predicted the failure of brittle materials with or without a discontinuity, such as a crack or notch, under uniaxial tensile loading. However, further testing is still needed in order to validate the robustness of Kwon's failure criteria. Due to an introduced notch and brittleness of the material, an investigation into the failure of bolt fastened poly(methyl methacrylate) (PMMA) and carbon fiber composites (CFC) provides an excellent opportunity to further validate Kwon's set of failure criteria and address failure commonly associated with mechanically fastened brittle materials. Therefore, the aim of this thesis is twofold, progress toward a unified failure criteria and accurately predict the failure of bolt fastened brittle materials.

A. BOLTED JOINTS

The joining of materials in structural design continues to be an ongoing engineering dilemma. Welding, fasteners, or adhesives may all achieve the desired structural integrity; however, other factors such as cost, time, and ease of replacement may also be necessary considerations when choosing an appropriate joining medium. In many instances, lower cost and ease of assembly, which results in higher productivity, are the predominant factors when selecting a joining method. Therefore, due to their relatively low cost and ease of assembly/disassembly, bolted joints are often utilized in many structural designs.

Rising fuel costs and environmental concerns have motivated engineers to replace commonly used metal structural materials with lightweight alternatives such as polymers and composites. In many cases, the lightweight component is incorporated into the design using bolts. As shown in Figure 1, there are various ways of bolting materials together. However, all require the removal of material to facilitate the insertion of the bolt. The resulting notch introduces stress concentrations in the surrounding material [7]. Due to the increased stress, failure of the component typically occurs at the site of the bolted joint.

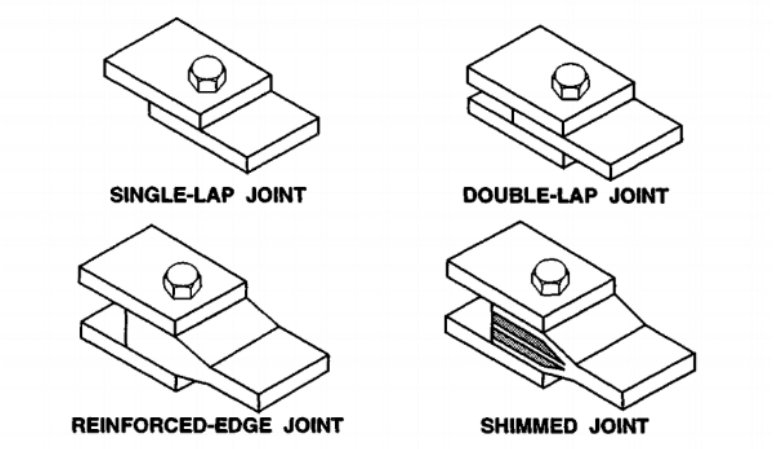

Figure 1. Bolted joints. Source: [3].

The failure of material at bolted joints can occur through several different modes. As shown in Figure 2, bolted joint failure in many materials, such as metals and composites, can occur by means of net-tension, shear-out, or bearing failure modes [7], [8]. In addition, Figure 2 illustrates that net-tension failure is the result of a normal stress, σ_x, and the decreasing width, w, of a fastened component. Shear-out failure is the result of a shear stress, τ_{xy}, and the decreasing geometrical parameter, e, which is the distance between the center of the hole and the edge of the fastened component. Lastly, bearing failure is the result of a radial stress, σ_{rr}. Typically, bolted joints composed of metal components tend to outperform joints constructed from other types of materials. An increase in performance may be attributed to the material's ductility [7]. Bolt fastened metals can alleviate stress concentrations through plastic deformation or dislocation motion. Unlike ductile materials, brittle materials cannot relieve stress through plastic deformation and failure of the material readily occurs at the joint.

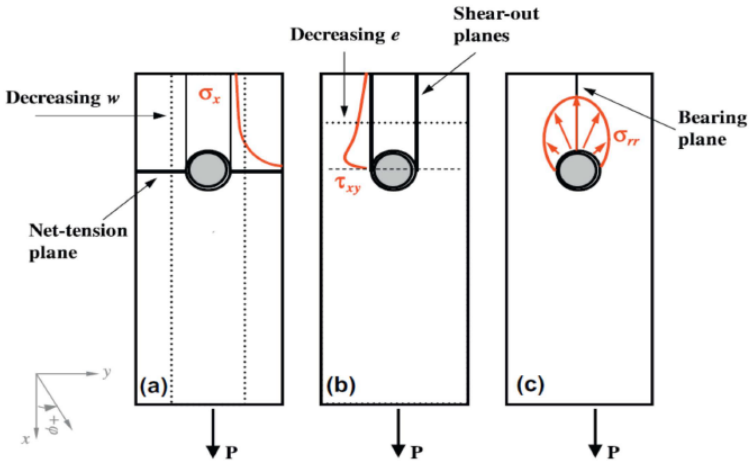

Figure 2. Bolted joint failure modes: (a) net-tension failure, (b) shear-out, and (c) bearing failure. Source: [7].

Examination of bolted joint failure provides an excellent opportunity to further investigate the mechanics of material fracture. Due to the nature of how loading is transferred between the bolt and the component, as shown in Figure 2, the component

material will experience tensile, compressive, and shear stresses. Essentially, upon loading, the bolt induces an elaborate stress field in the component material and fracture may occur in response to any of the previously mentioned stresses. The component material may also experience a variety of subcritical failure mechanisms which ultimately lead to one of the bolted joint failure modes. For example, a heterogeneous and anisotropic material, such as a composite, may experience numerous subcritical failure mechanisms due to how stress is transferred through the materials constituent phases. Thus, the composite material is able to relieve stress differently when compared with homogeneous and isotropic materials, which have physical properties that are the same in all directions [1]. A discussion of the failure mechanisms associated with CFCs is provided in the Composites section of this chapter.

B. POLYMERS

Following World War II, the field of material science was reinvigorated and further transformed by the introduction of synthetic polymers [2]. As mentioned previously, the need for lightweight cost-effective metal alternatives has led to many advances in synthetic polymers. Polymers can now be produced with a vast array of physical properties. As shown in Figure 3, polymers can fracture while deforming elastically, like ceramics, or, similar to many metal structures, initially elastically deform, yield, and then plastically deform until fracture. Although the stress-strain behavior of polymers may be similar to ceramics and metals, in most cases, polymers typically do not possess the same strength.

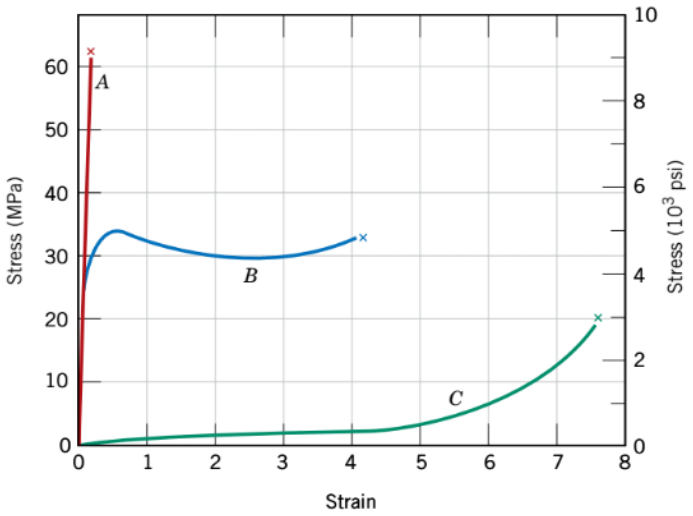

Figure 3. Stress-strain behavior of polymers: (a) brittle, (b) plastic, and (c) highly elastic polymers. Source: [2].

Thermoplastics, which soften when heated and harden when cooled, may experience ductile or brittle fracture [2]. Additionally, some thermoplastics may also possess a ductile-to-brittle transition temperature. Poly(methyl methacrylate) (PMMA) is a thermoplastic that has been extensively studied and characterized due to its utilization in many commercial and industrial applications [9]. As shown in Figure 4, PMMA is completely brittle at 4°C and becomes more ductile as temperature is increased. In Monterey, CA, where the Naval Postgraduate School (NPS) is located, the average temperature is approximately 15°C. For failure analysis experiments conducted at the NPS, the failure of PMMA results in a fracture that is predominately brittle in nature.

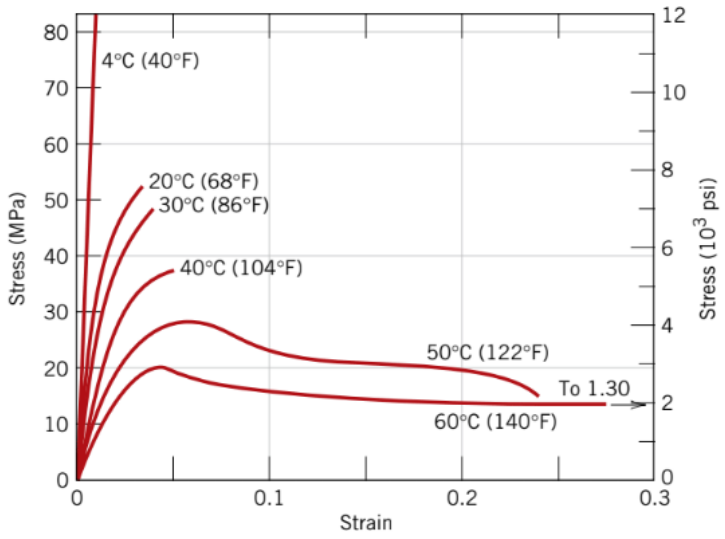

Figure 4. Temperature influence on PMMA stress-strain characteristics. Source: [2].

PMMA is readily used when evaluating the fracture characteristics of brittle materials [10]. In addition to PMMA fracturing in a brittle manner at room temperature, the material is relatively homogeneous and isotropic. Parts made for failure analysis can be easily constructed using a variety of machining or cutting methods. Also, due to the optical transparency of PMMA, cracks formed in the material can be easily observed. Therefore, a bolted joint constructed of PMMA provides an excellent model for evaluating the failure of bolted fasteners in a variety of brittle materials.

C. COMPOSITES

As described in Jones [3], "The word composite in the term composite material signifies that two or more materials are combined on a macroscopic scale to form a useful third material." The aim of designing a composite material is to create a single material that displays the desirable properties associated with each of the constituent or component materials [2], [3]. For example, fiberglass, a common structural material used in automobiles, aircrafts, and boats, is a composite material composed of a polymeric material that is embedded with glass fibers [2]. The glass fibers are strong, stiff, and brittle, whereas the polymer is lightweight and flexible. The combination of constituent

phases results in fiberglass being relatively strong, stiff, lightweight, and flexible. Similar to fiberglass, but typically more expensive, carbon fiber composite (CFC) is also a fiber-reinforced polymer. However, unlike fiberglass, which utilizes glass fibers to reinforce the polymer, CFCs have significantly stronger and stiffer carbon fibers [2].

In addition to a composite's constituent phases, strength and stiffness is also a function of applied stress orientation in relation to the materials principal coordinates [2], [3]. As shown in Figure 5, typical flat lamina associated with CFC consists of unidirectional or woven fibers. Using the unidirectional fiber image shown in Figure 5 as a reference, it is easy to imagine that strength and stiffness of the material is highest in the principal direction orientated along the length of the fiber. In many instances, and as shown in Figure 6, the CFC is a laminate constructed of multiple layers of laminae or plies which may be orientated in various configurations to achieve different physical properties. For example, for the same number of plies, the unidirectional layup shown in Figure 6 has greater in-plane strength and stiffness in the 0° direction when compared with the other layups shown. However, the multidirectional layup has the greatest degree of in-plane isotropy. Thus, from a design standpoint, what also makes CFCs so appealing is that they can be customized to meet the specific needs of their expected loading conditions.

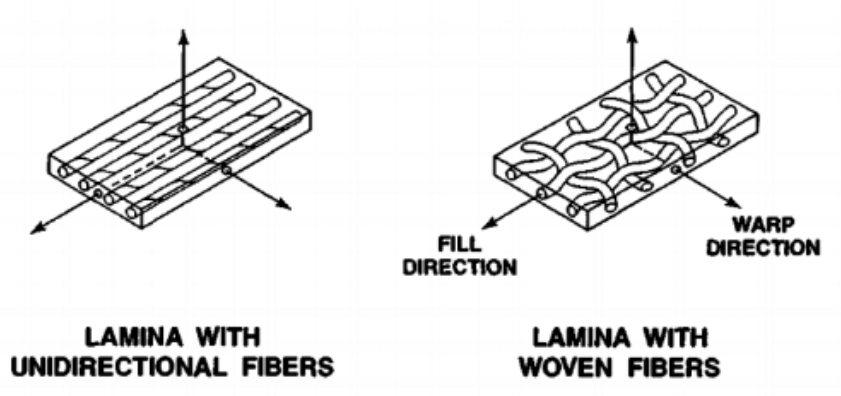

Figure 5. Two principal types of laminae. Source: [3].

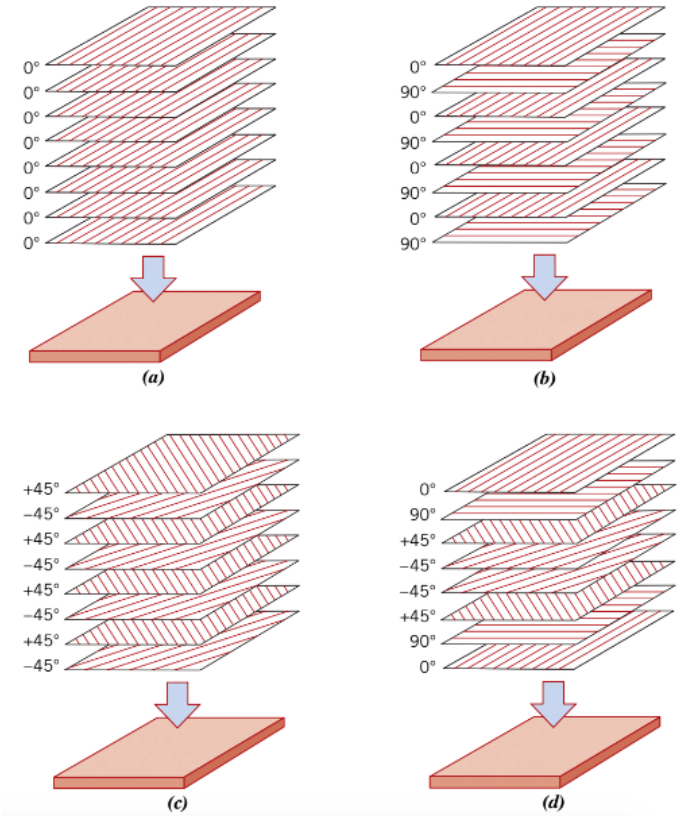

Figure 6. Layups for laminar composites: (a) unidirectional, (b) cross-ply, (c) angle-ply, and (d) multidirectional. Source: [2].

CFCs are currently used for a multitude of structural applications and the replacement of metal structural materials for CFCs continues to rise in many industries [2], [3], [7]. The increase in CFC utilization can be attributed to the materials superb physical and mechanical properties, as well as a reduction in manufacturing costs. CFCs have a greater strength/weight and stiffness/weight ratio than steel [11]. Essentially, the strength of steel can be achieved with only 20% of the weight. Additionally, advances in manufacturing and processing technologies are beginning to make CFCs more cost effective [12].

As CFCs become more prevalent in structural design it is inherently important to understand potential failure mechanisms. Failure of CFC material readily occurs near joining sites. The joining of a CFC structural element is typically accomplished with adhesives or bolted joints. CFCs naturally lend themselves to adhesive joints because

joining can be accomplished by using the same matrix that the original part was formed, with additional carbon fibers added for improved strength. However, adhesive joints require extensive preparation, and the part cannot be removed without destructive means. As previously mentioned, the bolted joint is a low-cost option that allows structural elements to be easily installed and removed. Unfortunately, creating the bolted joint requires cutting a notch in the material which generates stress risers that make the material susceptible to failure.

Examination of CFC bolted joint failure provides an excellent opportunity to explore many of the subcritical failure mechanisms associated with CFCs. Bolt fastened CFC typically experiences in-plane material failure as shown in Figure 2. However, it is important to note that failure of a joint by one of the shown failure modes is usually the result of a combination of subcritical failure or damage mechanisms [1]. As seen in Figure 7, failure of the material can occur through numerous subcritical damage mechanisms, such as fiber pull-out, fiber bridging, fiber/matrix debonding, fiber failure, matrix cracking, buckling, and delamination. Unlike, a brittle, homogeneous, and isotropic material, the CFC is able to relieve stress through a number of mechanisms. Therefore, another advantage of CFCs is that material failure is progressive and rarely occurs without warning.

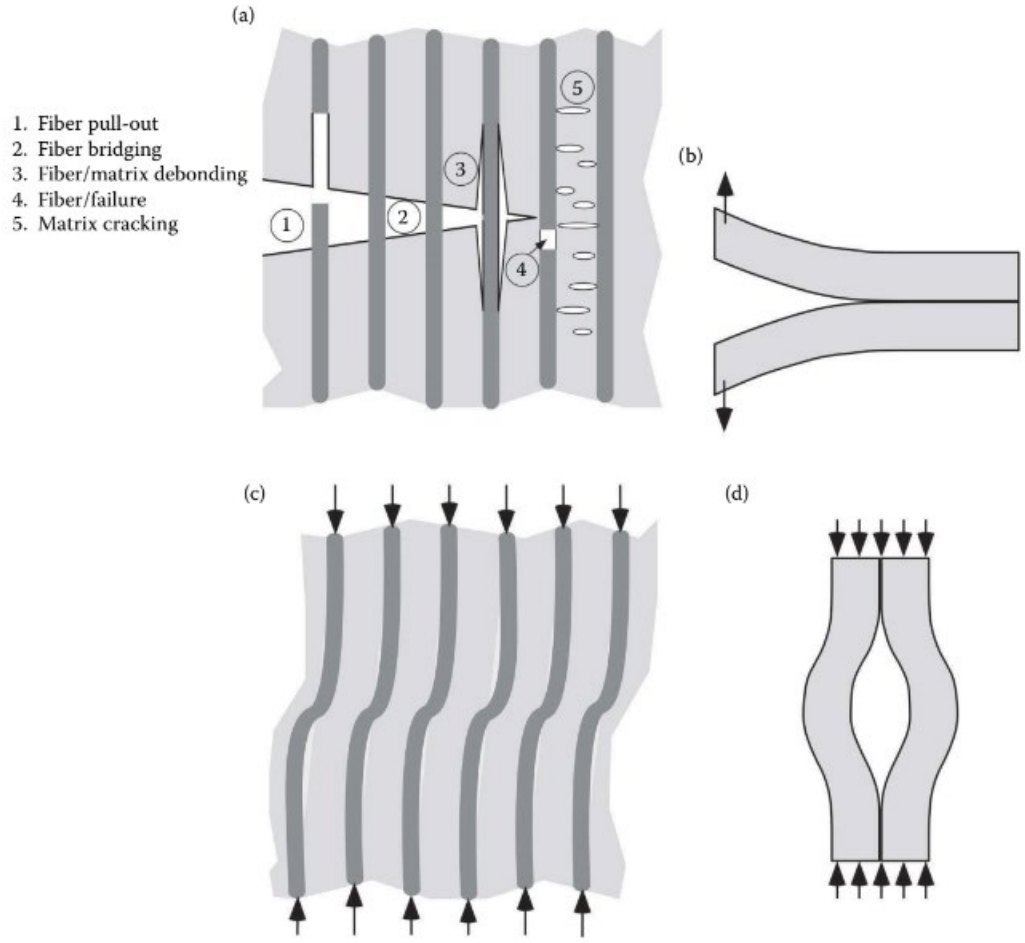

Figure 7. Examples of damage and fracture mechanisms in fiber-reinforced composites: a) in-plane damage, b) delamination, c) microbuckling, and d) buckling delamination. Source: [1].

Variations in CFC construction, such as ply layup, carbon fiber selection, and epoxy composition, all affect how stress is distributed throughout the material. Therefore, the failure mode as well as the subcritical failure mechanisms are all affected by any variation to the CFC design. Due to the many factors affecting the stress field induced in the material, it continues to be an ongoing challenge for engineers to accurately model and predict failure of a composite material.

D. FAILURE CRITERIA

A. A. Griffith, an English engineer, is largely credited for establishing the field of fracture mechanics in 1920 [1], [4]. Utilizing the first law of thermodynamics, Griffith

was the first to equate the strain energy associated with material failure to the energy needed to generate new surfaces [13]. In 1913, seven years prior to Griffith's published work, Charles E. Inglis published a paper which provided a two-dimensional solution for an elliptical hole or notch in an elastic material under tensile loading [1]. Assuming that the elliptical hole is not influenced by the rectangular plate boundaries, Inglis expressed the stress at the tip of the major axis of the ellipse, which is also the maximum stress in the material, as

$$\sigma_{MAX} = \sigma\left(1 + 2\sqrt{\frac{a}{\rho}}\right), \tag{1}$$

where

$$\rho = \frac{b^2}{a}. \tag{2}$$

In Equation (1), σ_{MAX} is the maximum stress in the material located at the tip of the major axis and σ is the stress associated with the tensile load applied at the boundaries perpendicular to the major axis. In Equation (2), ρ, the radius of curvature, is a function of b, which is half the length of the minor axis, and a, which is half the length of the major axis. Inglis' equation provides a good solution for an elliptical notch as long as the radius of curvature does not become too small. As seen in Equation (1), as ρ becomes infinitely small, or the elliptical notch begins to resemble a crack, the maximum stress becomes infinitely large. Therefore, according to the equation, an infinitesimally small load applied to a material with a small crack should result in material failure. The paradox of Inglis' equation motivated Griffith to create a fracture theory that is based on energy rather than local stress [1].

Griffith's theory assumes that brittle materials contain minute cracks, and that fracture of the material requires sufficient energy to grow and propagate these cracks [1], [13]. Under equilibrium conditions, the energy balance equation associated with Griffith's work can be expressed as

$$\frac{dE}{dA} = \frac{d\Pi}{dA} + \frac{dW_s}{dA} = 0, \tag{3}$$

where E is the total energy, A is the crack area, Π is the potential energy associated with internal strain energy and externally applied forces, and W_s is the work required to generate new crack surfaces [1]. Utilizing Inglis' work, Griffith was able to solve for the potential energy and the work required to generate new crack surfaces, which he expressed in terms of surface energy of the material. After proper substitution into Equation (3), the Griffith equation is

$$\sigma_f = \left(\frac{2E\gamma_s}{\pi a} \right)^{\frac{1}{2}}, \tag{4}$$

where σ_f is the failure stress, E is the Young's modulus, γ_s is the specific surface energy associated with the material, and a is half the length of an internal crack. Griffith primarily worked with glass, an ideally brittle solid, and Equation (4) correctly modeled his experimental results. However, when Griffith's equation is applied to other materials, such as metals, the equation severely underestimates the fracture energy [1].

It was not until 1948, over twenty years after Griffith's published work, that the discrepancy in Griffith's equation was addressed. G. R. Irwin modified Griffith's equation by adding a variable to account for the energy dissipation associated with plastic deformation in metals [1]. Essentially, Irwin's work revealed that Griffith's equation could be expressed as

$$\sigma_f = \left(\frac{2Ew_f}{\pi a} \right)^{\frac{1}{2}}, \tag{5}$$

where w_f is the fracture energy, which is a variable that accounts for any type of energy dissipation.

In the years that followed, Irwin continued to expand upon Griffith's model. In 1957, with the aid of his colleagues at the U.S. Naval Research Laboratory, Irwin

introduced a new parameter and material property, stress intensity factor (SIF) and fracture toughness [14], [15]. Unlike the Griffith method, which does not consider the local stress at the crack tip, Irwin's model utilizes a crack tip stress field analysis. His work demonstrated that there is a stress intensity associated with crack shape and loading geometry [15]. As shown in Figure 8, loading can be applied to a crack by three modes: opening, in-plane shear, and out-of-plane shear. Additionally, the SIF, K, describes the state of stress or stress intensity near the crack tip or notch. Typically, the SIF is denoted as K_I, K_{II}, or K_{III} to denote the mode of loading [1]. For example, for a through crack in a linear elastic finite plate undergoing purely Mode I loading the SIF is given as

$$K_{(I,II,III)} = Y\sigma\sqrt{\pi a}\,, \tag{6}$$

where Y is a constant depending on geometry and mode of loading, σ is the applied stress, and a is the crack length. The SIF calculated when a crack begins to propagate in a material is known as fracture toughness, K_c [13]. Therefore, if the SIF is greater than equal to the fracture toughness, material failure is expected to occur. Lastly, Irwin was able to equate SIFs and Griffith's criterion by

$$G = \frac{K^2}{E}, \tag{7}$$

where G is the energy release rate, obtained through manipulation of Equation (4), K is the SIF, and E is the Young's modulus. Although Irwin was able to show equivalence between the models, the SIF parameter developed by Irwin, is much easier to apply to engineering problems and is a fundamental concept used in linear elastic fracture mechanics (LEFM).

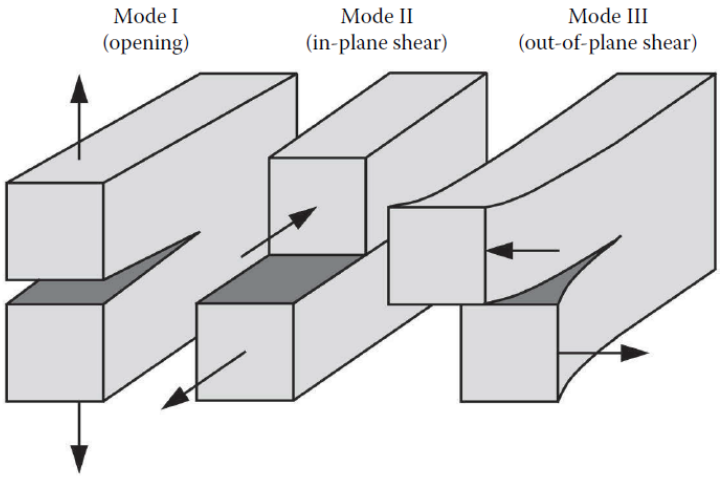

Figure 8. Three modes of loading that can be applied to a crack. Source: [1].

The early work of Griffith and Irwin falls under a subdivision of fracture mechanics, known as LEFM. As the name implies, the concepts of LEFM are only applicable to linear elastic materials or materials where plastic deformation near the crack tip is small. Essentially, LEFM ceases to be valid and breaks down as materials become more ductile. Although, LEFM is only valid for elastic materials, subsequent research in the field of fracture mechanics has all been predicated on LEFM. For example, elastic-plastic fracture mechanics, dynamic fracture mechanics, viscoelastic fracture mechanics, and viscoplastic fracture mechanics are all subdivisions of fracture mechanics that are rooted in LEFM [1]. Therefore, a good understanding of LEFM is necessary to understand more advanced and newly proposed facture mechanics concepts.

Following the early years of fracture mechanics, a substantial number of models, theories, and computational methods have been developed to predict material failure in brittle and quasi-brittle materials, such as PMMA and CFC. In most cases, the proposed models and theories can only predict failure under very specific conditions. However, ongoing research continues to bridge the gaps between models and attempts are being made to move toward a more unified set of failure criterion.

The theory of critical distances (TCD) uses a characteristic material length parameter, known as critical distance, to predict brittle fracture of a material that contains either a notch or crack [16]. Critical distance is a function of the materials facture

toughness and a critical stress. As previously mentioned, LEFM is based on the propagation of a preexisting crack. Therefore, if the failure of an elastic material containing a notch needs to be determined, notched methods, such as Inglis' work, are utilized. However, notched methods begin to provide inaccurate predictions when the notch sharpens or begins to resemble a crack. TCD uses the elastic stress information in a critical region, adjacent to the notch tip and defined by the critical distance, to determine when the material will fail [16]. The point and average stress models are the two most commonly used approaches for analyzing the stress information in the critical region. The point stress model assumes that failure will occur when the stress at a point, located some distance away from the notch tip, reaches the critical stress value, whereas the average stress model predicts failure will occur when the average stress in the critical region reaches the critical stress value [17]. Furthermore, the concepts associated with TCD are also embodied in the method of finite fracture mechanics (FFM).

FFM modifies the traditional work of Griffith's energy balance criterion [18]. As shown in Equation (3), Griffith's work equates infinitesimal changes in potential energy to infinitesimal crack extension. FFM modifies the relationship to only allow for finite crack extension. As a result of the modification, Griffith's equation, Equation (4), is expressed as

$$\sigma_f = \sqrt{\frac{G_c E}{\pi\left(a + \Delta a/2\right)}}, \tag{8}$$

where G_c is the critical energy release rate, which equals to $2\gamma_s$ in Equation (4), and $\Delta a/2$ is an additional term associated with the finite change in crack length. The term $\Delta a/2$ is also related to the critical distance concept previously discussed. In addition to being unable to provide accurate predictions for notches, LEFM cannot predict the behavior of short cracks. When LEFM is utilized for brittle materials with short cracks, the predicted value is higher than the actual fracture strength of the material. FFM, through the modification of Griffith's equation, is able to provide fairly accurate predictions for notches and cracks of various length in brittle materials under monotonic

loading. Lastly, FFM can be shown to give predictions similar to the average stress model in the TCD.

The models and theories discussed thus far make up only a small fraction of the work that has been conducted in the field of fracture mechanics, and, for the most part, have only applied to brittle, isotropic materials. As is the case with most research, newly developed theories are tested under very specific conditions. Oftentimes, when the proposed theory is applied beyond the scope of the initial work unfavorable results occur and the theory must be modified or rejected. The same has been true for fracture mechanics. Changes to loading conditions, material constraints, material geometry, and material properties have all affected how well a given theory predicts material failure. Therefore, if material failure must be predicted, the current practice is to select the theory or failure criteria that has been shown to provide the most accurate results for a given set of conditions.

Kwon seeks to eliminate the need for multiple failure criteria when predicting the failure of a brittle material. In [5], Kwon proposes a unified set of failure criteria which can predict the failure of a brittle material regardless of whether there is a discontinuity, such as a notch or crack, present in the material. Unlike the previously discussed models that use a critical stress value located some distance away from the site of crack initiation, Kwon suggests analyzing the stress and stress gradient at the location of initial crack formation to determine if material failure is feasible. The two conditions that must simultaneously be met for material failure are expressed as follows:

$$\sigma_l \geq \sigma_f . \tag{9}$$

$$\frac{\sigma_l^3}{2E}\left|\frac{d\sigma_l}{ds}\right|^{-1} \geq \kappa_{fail} . \tag{10}$$

Equation (9) states that the local stress, σ_l, must be greater than or equal to the failure stress of the material, σ_f, which can be obtained from a standard tensile test.

Equation (10) is associated with the stress gradient. In Equation (10), $\left|\frac{d\sigma_l}{ds}\right|$ is the magnitude of the normalized stress gradient, which is calculated by dividing the stress values along the failure path by the local/maximum stress, E is the Young's modulus, and κ_{fail} is the failure value, which is a material constant. The failure value of a material can be obtained from a tensile test of a notched material sample and a finite element analysis (FEA). As discussed in Kwon [5], early results suggest that in addition to the failure location, the newly proposed set of failure criteria may also predict the failure path.

In [6], further analysis is performed to evaluate the effectiveness of Kwon's failure criteria. In addition to various shaped notches in PMMA, an anisotropic material, CFC, was also evaluated using the new set of failure criteria. The new failure criteria provided comparable failure stress predictions to the experimental results for both PMMA and CFC, which consisted of symmetric cross-ply (CP) and quasi-isotropic (QI) layups. In addition, the failure path coincided with the shallowest stress gradient emanating from the local/maximum stress.

So far, Kwon's proposed set of failure criteria has shown the ability to accurately predict the failure location and direction of a brittle material, regardless of notch shape, while under uniaxial tensile loading. However, further evaluation of Kwon's failure criteria is still necessary to validate current work and further explore its applicability as a unified failure criterion. This thesis will further examine Kwon's set of failure criteria by attempting to predict the failure location and direction of bolt fastened PMMA and CFC.

THIS PAGE INTENTIONALLY LEFT BLANK

II. EXPERIMENTAL SETUP

A. MATERIALS

1. PMMA

Utilizing a waterjet cutter, several specimens were machined out of commercially available sheets of PMMA. The sheets were nominally 30.5 cm x 61.0 cm x 0.45 cm; however, the actual thickness of the sheets ranged from 0.39 cm to 0.45 cm. Therefore, there was a small but noticeable thickness variation amongst the specimens. As shown in Figures 9 through 14, six different parts were fabricated in an attempt to vary the location of fracture initiation and direction of crack propagation. In addition, five specimens of parts P1through P3 and ten specimens of parts P4 through P6 were manufactured. Lastly, the material properties of the PMMA used were obtained from tensile tests and are shown in Table 1.

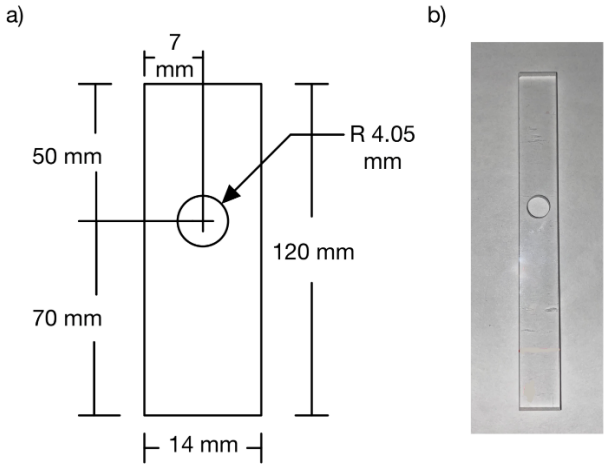

Figure 9. PMMA part 1 (P1): a) schematic and b) actual part

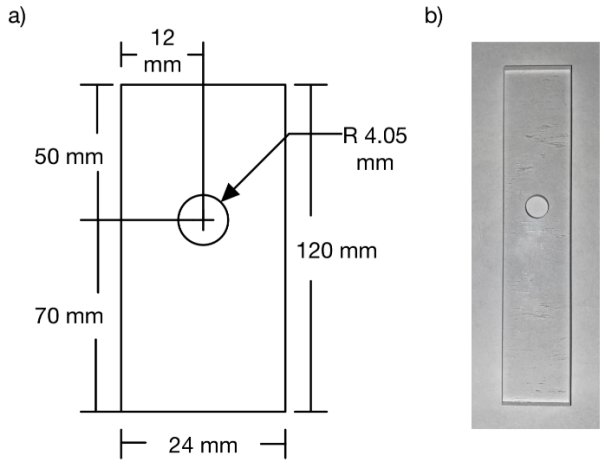

Figure 10. PMMA part 2 (P2): a) schematic and b) actual part

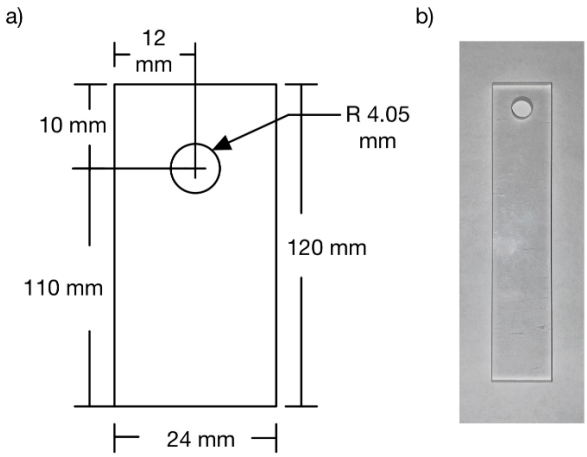

Figure 11. PMMA part 3 (P3): a) schematic and b) actual part

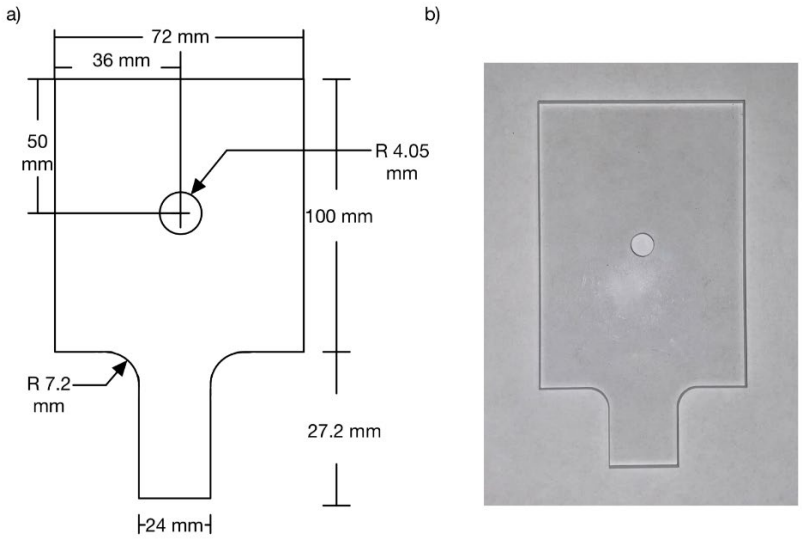

Figure 12. PMMA part 4 (P4): a) schematic and b) actual part

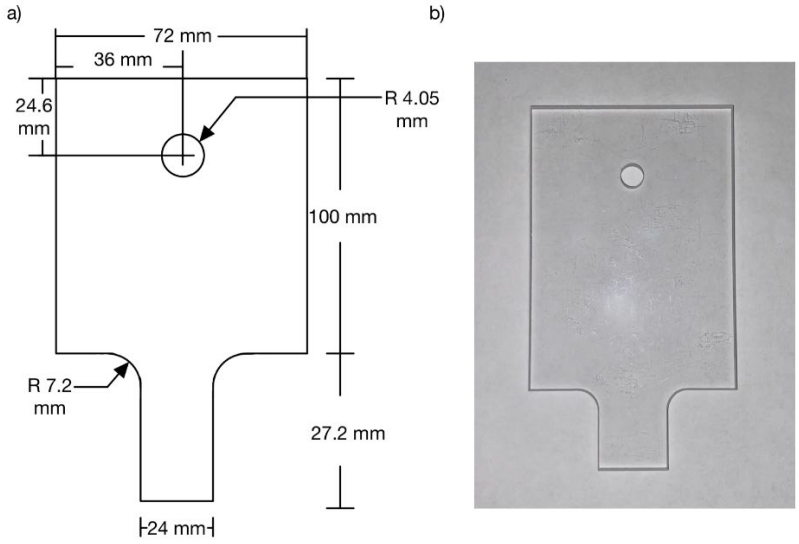

Figure 13. PMMA part 5 (P5): a) schematic and b) actual part

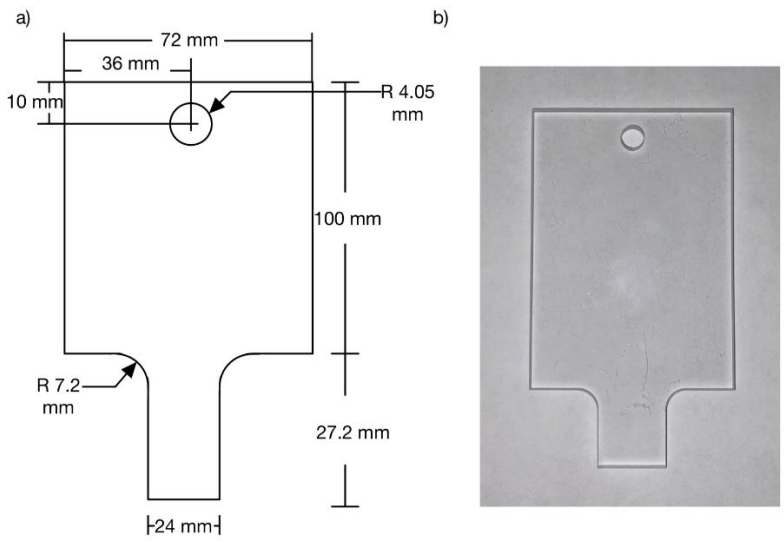

Figure 14. PMMA part 6 (P6): a) schematic and b) actual part

Table 1. PMMA material properties

Property	Value	Unit
Density	1180	kg/m^3
Young's Modulus	2619.6	MPa
Poisson's Ratio	0.33	
Bulk Modulus	2568.3	MPa
Shear Modulus	948.8	MPa
Tensile Yield Strength	58.5	MPa

2. CFC

Two different carbon fiber epoxy laminate sheets were obtained from DragonPlate, a commercial manufacturer and distributor of CFCs. As previously mentioned, laminate layup affects the stress distribution in a composite material; therefore, cross-ply (CP), $[90/0/90]_s$, and quasi-isotropic (QI), $[90/0/45/–45/90/0]_s$, laminates were selected for evaluation. A more detailed description of the laminate layups as well as the manufacturers material specifications are provided in Tables 2 through 4 [19], [20]. Additionally, tensile tests were conducted on single ply sheets of unidirectional prepreg composite in order to obtain the material properties for an

individual ply or lamina within the laminate. The material properties for a unidirectional prepreg lamina are shown in Table 5.

Table 2. Cross-ply stacking sequence

Cross-ply Plies
90°
0°
90°
90°
0°
90°
Ply thickness ~ 0.29464 mm

Table 3. Quasi-isotropic stacking sequence

Quasi-isotropic Plies
90°
0°
45°
-45°
90°
0°
0°
90°
-45°
45°
0°
90°
Ply thickness ~ 0.14732 mm

Table 4. DragonPlate CFC laminate specifications. Adapted from [19], [20].

Cross-ply Unidirectional Prepreg Sheet							
SKU	Sheet Size	Thickness	UTS	Modulus	Resin	Density	Tg
FDPLHP02T*90*1212	30.5 cm x 30.5 cm	0.16 cm	4826 MPa	234 GPa	NCT 304-1	1550 kg/m^3	121 °C
Quasi-isotropic Unidirectional Prepreg Sheet							
SKU	Sheet Size	Thickness	UTS	Modulus	Resin	Density	Tg
FDPLHP02T1212	30.5 cm x 30.5 cm	0.16 cm	4826 MPa	234 GPa	NCT 304-1	1550 kg/m^3	121 °C

Table 5. CFC lamina material properties

E_{11} (GPa)	E_{22} (GPa)	E_{33} (GPa)	υ_{12}	υ_{23}	υ_{13}	G_{12} (GPa)	G_{23} (GPa)	G_{13} (GPa)
111.60	7.61	7.61	0.2053	0.3340	0.2053	2.89	2.88	2.89

In [21], the authors investigated the bearing strength of mechanically fastened carbon fiber epoxy laminates. They concluded that geometrical parameters such as edge distance to hole diameter (*e/d*) and width to hole diameter (*w/d*) affect the failure mode of pin loaded laminates. As shown in Figure 15, edge distance, *e*, is the distance between the center of the hole and the edge of the specimen. For the purposes of this research, a net-tension failure mode was desired since it also provides the greatest likelihood of observing all the previously mentioned CFC subcritical failure mechanisms. According to [21], net-section failure occurred in $[0/45/90/–45]_s$ laminate when the *w/d* was less than 2. Therefore, a *w/d* of 1.75 was utilized in the design of CFC parts.

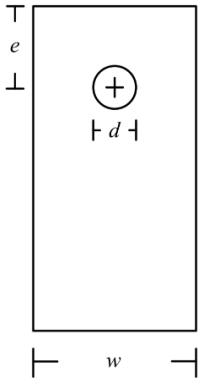

Figure 15. Geometrical parameter reference

Similar to the discussion of PMMA specimen fabrication, a waterjet cutter was also utilized to machine out parts from sheets of CFC. Four different parts were constructed from the CP and QI laminates. As shown in Figure 16, the dimensions of the four parts are the same, but the stacking sequence is different. Essentially, the first part was machined, then the sheet was rotated by 90º, and the second part was machined. The

result is four parts consisting of $[90/0/90]_s$, $[0/90/0]_s$, $[90/0/45/–45/90/0]_s$, and $[0/90/–45/45/0/90]_s$ layups. A total of 20 CFC specimens, five of each part, were manufactured.

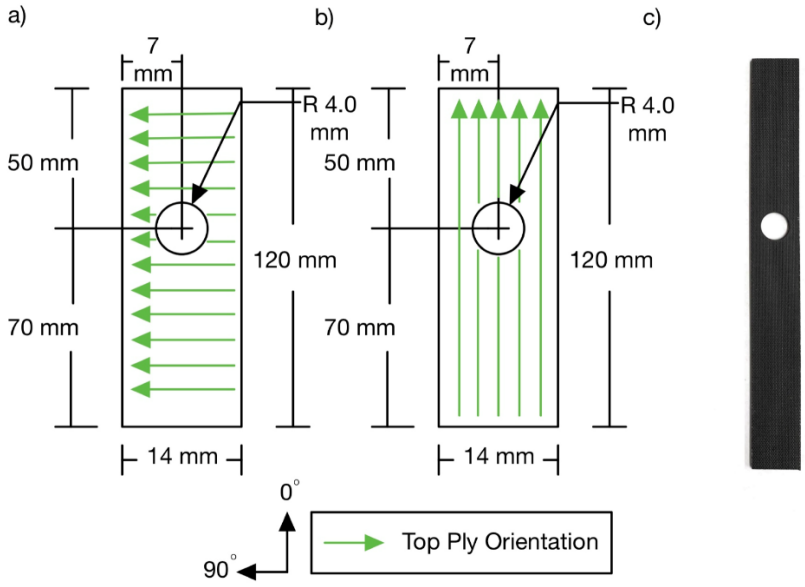

Figure 16. CP and QI parts: a) C1 and Q1schematic, b) C2 and Q2 schematic, and c) actual part

3. Adapter

In order to simulate the static loading on PMMA and CFC specimens by a bolt, an INSTRON 5982 universal testing machine and steel adapter were employed. As shown in Figure 17, the steel adapter was fabricated from a 45.72 cm x 2.54 cm x 0.495 cm steel bar. The adapter transfers load from the INSTRON 5982 to a shoulder bolt which is in contact with the PMMA or CFC specimen. Essentially, the INSTRON 5982 and steel adapter are used to simulate the in-plane loading associated with the middle section of a double-lap bolted joint (shown in Figure 1).

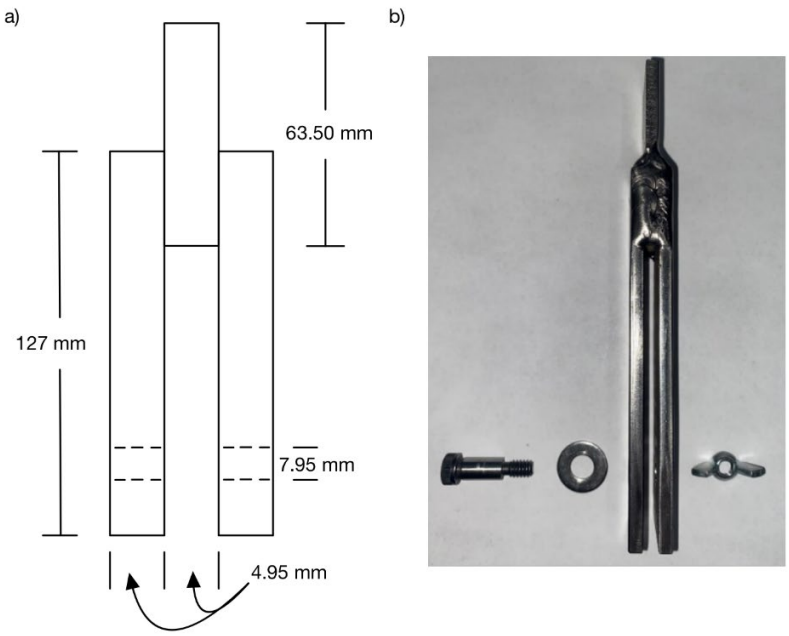

Figure 17. Steel adapter used to simulate bolted joint loading: a) adapter schematic and b) actual adapter with shoulder bolt

B. TEST EQUIPMENT

The INSTRON 5982 universal testing machine was the only test equipment used in this study. It is an electromechanical testing machine capable of performing a variety of mechanical tests, such as tensile, compression, and cyclic, with a maximum force capacity of 100 kN [22]. The tensile test mode was used in conjunction with the steel adapter to apply uniaxial loading to the PMMA and CFC specimens. In addition to initiating material failure, the tensile test provides important specimen loading information, such as time, force, and displacement.

C. TEST SETUP AND EXECUTION

Failure of the PMMA and CFC specimens was achieved by conducting tensile tests using the INSTRON 5982. As shown in Figure 18, the steel adapter and test specimens were loaded into the INSTRON 5982 by gripping 25 mm, from the top edge, of the adapter and 20 mm, from the bottom edge, of the specimen. A bubble level was used to ensure that both the adapter and specimen were aligned vertically in the machine. Upon utilization of the bubble level, it was determined that parts with a 24 mm wide grip

section would not align vertically unless they slightly protruded out of the lower grip. Therefore, as shown in Figure 19, for parts with a 24 mm wide grip section, the actual area secured by the lower grip was 20 mm x 21 mm. Additionally, all tensile tests were conducted using a test rate of 2 mm/min.

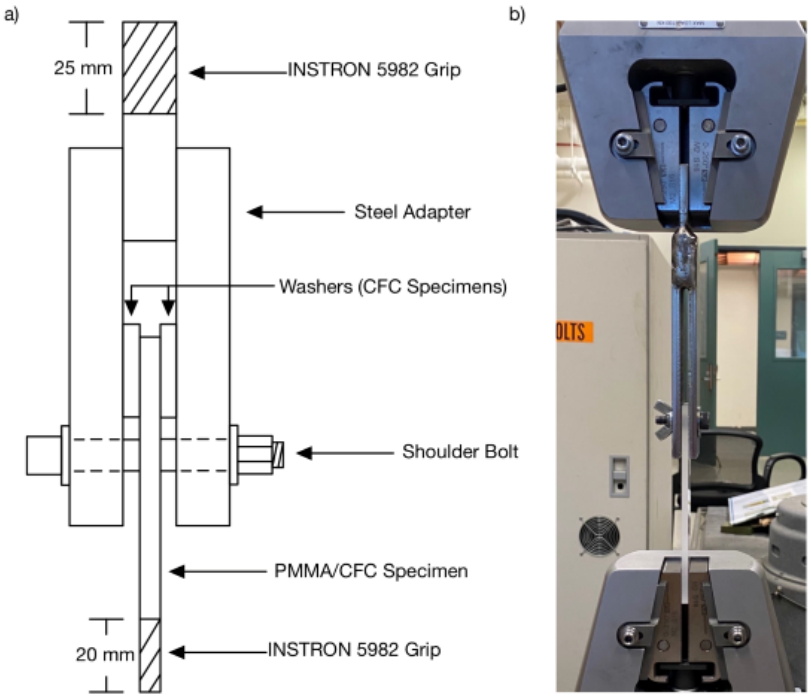

Figure 18. Bolted joint test setup: a) schematic and b) actual setup with P3

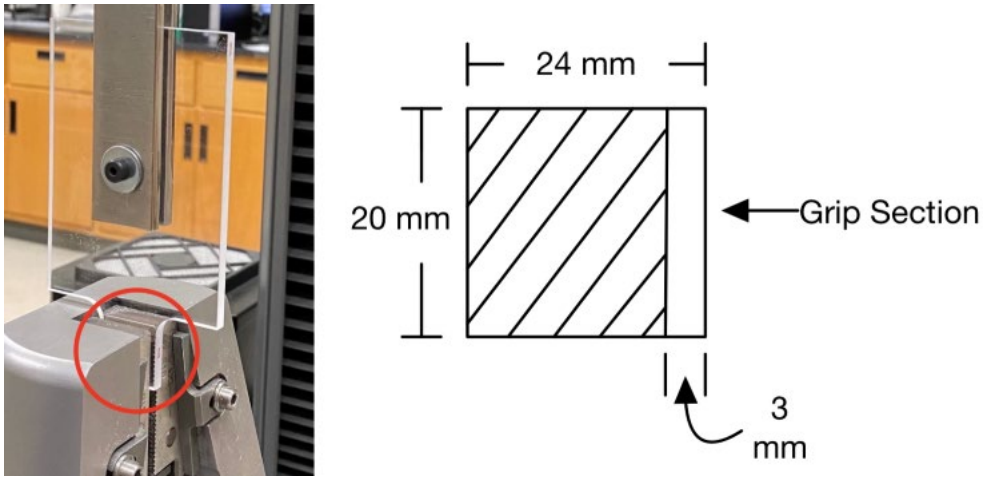

Figure 19. Tensile test secured area for parts with 24 mm wide grip section

1. PMMA - Parts 1 through 3

Five specimens of P1, P2, and P3 were manufactured. For each part, tensile or failure tests were conducted using 8 mm, 6 mm, and 5 mm shoulder bolts. Three tests were conducted using the 8mm bolt, and one test was conducted for both the 6 mm and 5 mm bolts. Tensile testing concluded upon initial failure.

2. PMMA – Parts 4 through 6

Ten specimens of P4, P5, and P6 were manufactured. For each part, tensile tests were conducted using an 8 mm and 5 mm shoulder bolt. Five tests were conducted with each of the bolts. Tensile testing concluded upon initial failure.

3. CP and QI Parts

Five specimens of C1, C2, Q1, and Q2 were manufactured. Unlike the PMMA specimens, tensile tests were conducted using only the 8 mm shoulder bolt. In addition, as shown in Figures 18 and 20, washers were placed between the assembly and composite in order to keep the specimen vertically aligned and reduce bending during the tensile test. The washers were not placed on the bolt because early trial tests showed an increase in failure strength due to a clamping effect as the material compressed and pushed out against the adjacent washers. For the purposes of this study, failure of the material was designated as the point of initial reduction in strength during tensile testing. The majority of tensile tests concluded upon initial failure. However, one specimen of each of the four parts was allowed to progress further than the initial reduction in strength in an attempt to completely fracture the material.

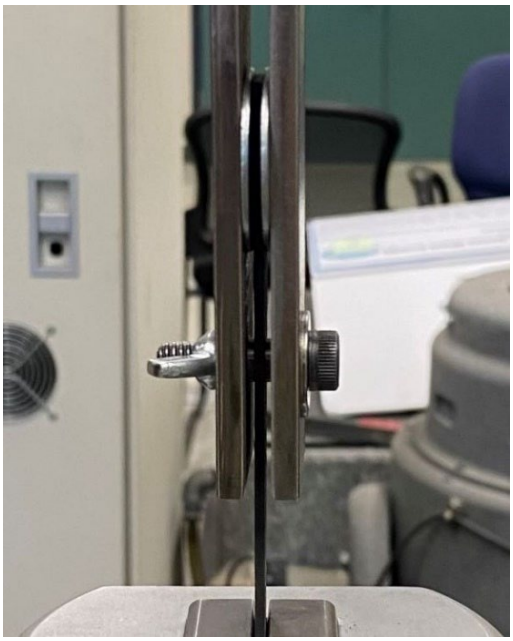

Figure 20. CFC test setup with washers

THIS PAGE INTENTIONALLY LEFT BLANK

III. NUMERICAL ANALYSIS

A finite element analysis (FEA) of all manufactured parts was conducted using Ansys, a FEA software package, and SolidWorks, a 3D computer-aided design (CAD) software. Essentially, all of the PMMA parts, CFC parts, and bolts used in the tensile/failure tests were initially modeled in SolidWorks and then imported into Ansys for FEA.

A. PMMA

1. 3D Models

As previously mentioned, the PMMA parts and shoulder bolts were modeled in SolidWorks. The PMMA parts were modeled with the dimensions provided in Figures 9 through 14. In addition, due to the variation in thickness amongst the specimens, a 4 mm thickness was used for all parts. As shown in Figure 21, the three shoulder bolts were all modeled with a length of 4.95 mm, the portion of the bolt between the two vertical sections of the assembly, and a measured diameter of 7.87 mm, 5.97 mm, and 4.95 mm.

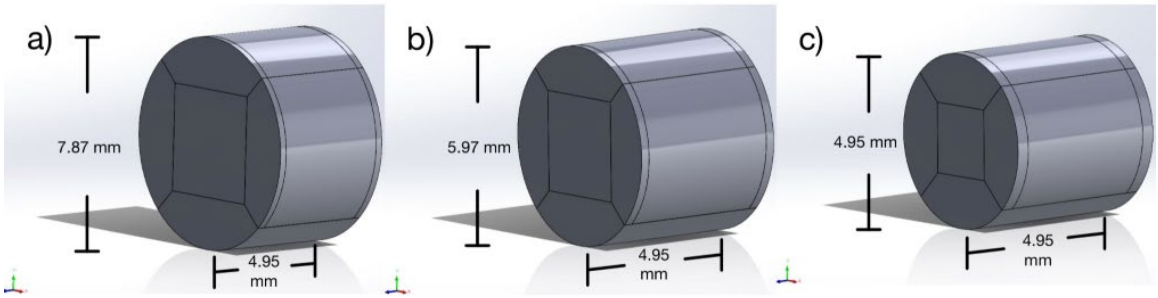

Figure 21. 3D shoulder bolt models: a) 8 mm, b) 6 mm, and c) 5 mm

2. Ansys

First, the material properties for PMMA, shown in Table 1, were input into Ansys's engineering data. Structural steel, which is provided in Ansys's material library, was used for all shoulder bolts. Two mechanical models in Ansys workbench were utilized: one for the PMMA part and one for the shoulder bolt. A PMMA part and

shoulder bolt, modeled in SolidWorks, were then imported into their respective module. For each module, the appropriate material was selected, and an adequate mesh was generated.

Due to the static nature of tensile tests, a static structural module was selected and added to the workbench. As shown in Figure 22, the two mechanical models were linked to the static structural module in the Ansys workbench in order to perform the static loading analysis. Then, as seen in Figure 23, a contact pair was created between the PMMA part and the bolt. A frictional contact was selected, and based on [23], [24], a frictional coefficient of 0.2 was applied. Additionally, a Normal Lagrange contact formulation was utilized.

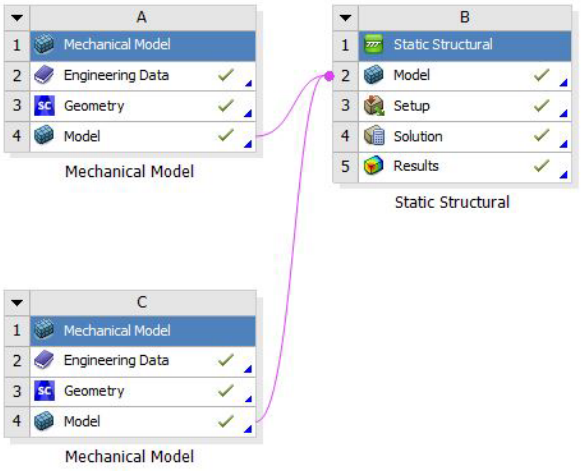

Figure 22. Standard Ansys workbench used to model a bolted joint

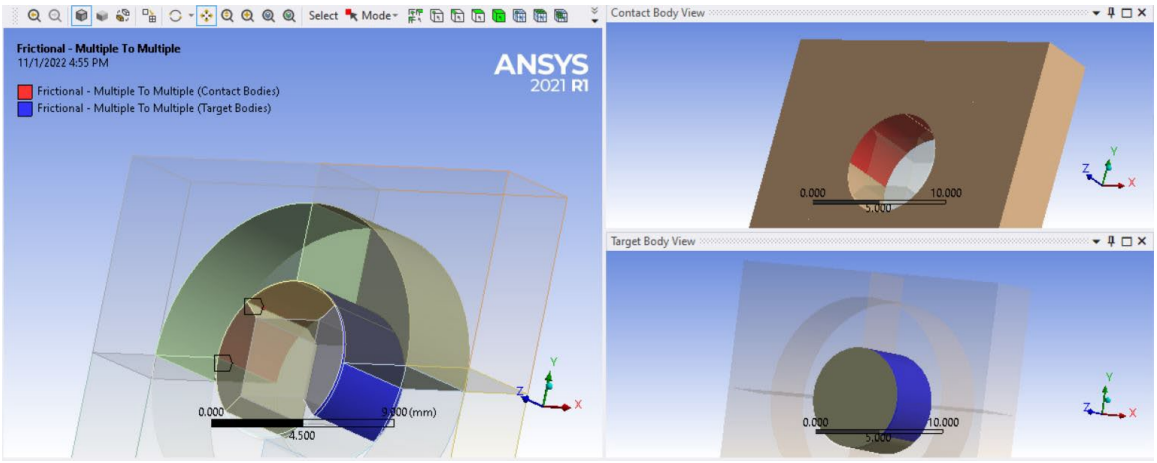

Figure 23. Ansys contact pair

Next, material constraints and loading were applied to the model. As shown in Figure 24, fixed supports were added at both ends of the modeled bolt; a force, obtained from tensile/failure tests, was applied to the bottom face of the part; and a remote displacement, which allowed only vertical motion of the part, was added to the same face as the force. As previously discussed, there was a small variation in the way specimens with a 24 mm grip section were secured in the INSTRON 5982. As result, and shown in Figure 25, the force and remote displacement were applied to a portion of the bottom face for parts with a 24 mm wide grip section, whereas the entire bottom face was assigned for parts with a 14 mm wide grip section.

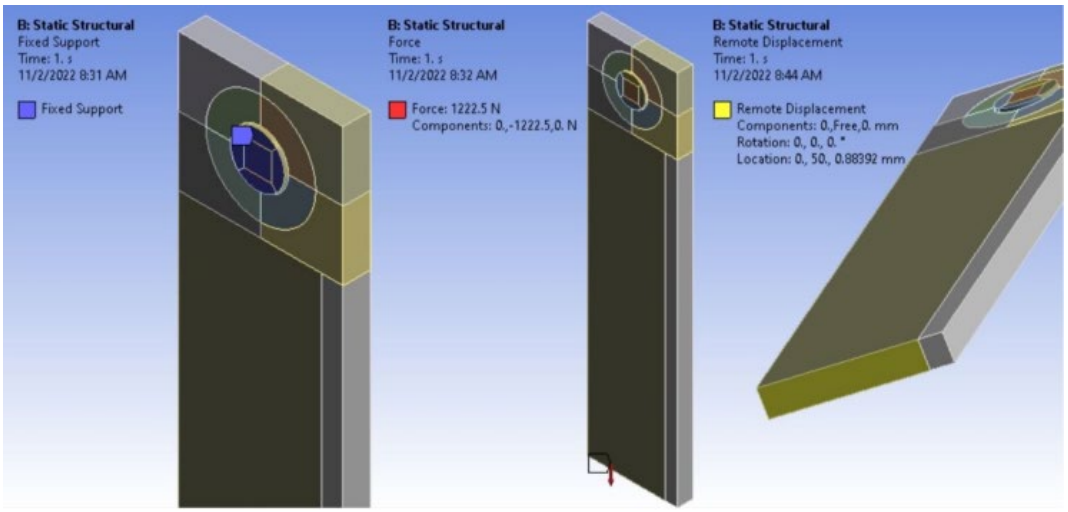

Figure 24. Bolted joint boundary conditions in Ansys

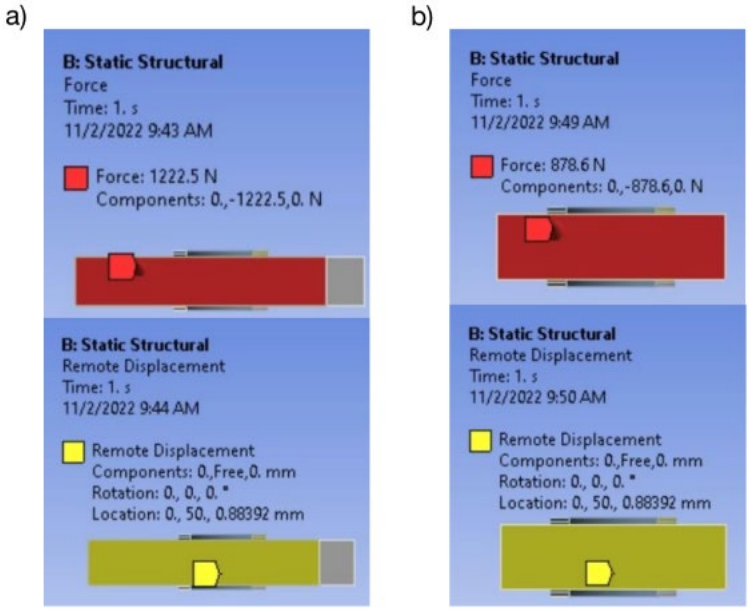

Figure 25. Force and remote displacement: a) 24 mm grip section and b) 14 mm grip section

Lastly, the model was solved, and the results were validated. Following solution convergence, penetration of the contact pair was examined to ensure minimal penetration between adjacent surfaces. A mesh sensitivity study was also conducted. Namely, more refined meshes were applied to the model and minimal stress variation was observed. Fujifilm Prescale, a pressure paper, was also used to capture the contact area between P6

and the 5 mm bolt during tensile/failure testing. As shown in Figure 26, the Fujifilm Prescale and the Ansys model produced similar contact areas. Aside from the Fujifilm Prescale, the described modeling sequence was carried out for all PMMA part and bolt combinations.

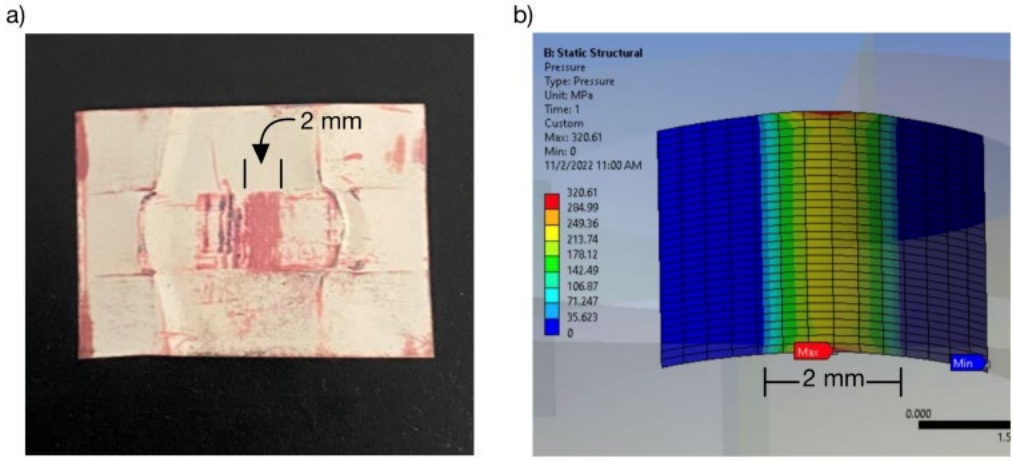

Figure 26. Contact area of P6 and 5 mm shoulder bolt: a) Fujifilm Prescale and b) Ansys model

B. CFC

1. 3D Models

CFC parts were modeled in SolidWorks using the dimensions shown in Figure 16 and a thickness of 1.768 mm. The 8 mm bolt used for PMMA tensile tests was also used for CFC tensile tests; therefore, the modeled bolt described in the PMMA 3D Models section was also utilized for CFC bolted joint modeling.

2. Ansys

a. Homogenized Model

Similar to Kwon et al. [6], a macromechanical approach was used to model the CP and QI laminate parts. More specifically, the classical lamination theory was used to smear the material properties associated with each lamina into a single homogenized layer [3], [6]. Utilizing MATLAB, a function was created to generate the effective elastic

material properties of the laminate. The function transforms a compliance matrix associated with the local coordinate system of a lamina to a compliance matrix associated with the global coordinate system of the laminate. Once all compliance matrices are properly transformed to the global coordinate system, Equation (11) is utilized to smear or average the compliance matrices into a single effective compliance matrix. Then the effective elastic material properties are extracted from the effective compliance matrix terms. As shown in Table 6, three sets of smeared material properties were required for the modeling of CFC parts. Unlike the CP parts, only one set of effective material properties were needed for the QI parts, since the material properties remain constant when the laminate is rotated 90 degrees.

$$\left[\bar{S}\right] = \frac{1}{T}\sum_{i=1}^{n}\left[S\right]_i t_i \,, \tag{11}$$

where $\left[\bar{S}\right]$ is the effective compliance matrix, T is the total thickness of the laminate, n is the number of lamina, $\left[S\right]_i$ is the transformed compliance matrix of the ith lamina, and t is the thickness of the ith lamina.

Table 6. Homogenized material properties for CP and QI parts

Cross-ply: $[90/0/90]_s$								
E_{11} (GPa)	E_{22} (GPa)	E_{33} (GPa)	υ_{12}	υ_{23}	υ_{13}	G_{12} (GPa)	G_{23} (GPa)	G_{13} (GPa)
76.94	42.27	7.61	0.1415	0.2911	0.2482	2.89	2.88	2.89
Cross-ply: $[0/90/0]_s$								
E_{11} (GPa)	E_{22} (GPa)	E_{33} (GPa)	υ_{12}	υ_{23}	υ_{13}	G_{12} (GPa)	G_{23} (GPa)	G_{13} (GPa)
42.27	76.94	7.61	0.0778	0.2482	0.2911	2.89	2.89	2.88
Quasi-isotropic: $[90/0/45/-45/90/0]_s$ and $[0/90/-45/45/0/90]_s$								
E_{11} (GPa)	E_{22} (GPa)	E_{33} (GPa)	υ_{12}	υ_{23}	υ_{13}	G_{12} (GPa)	G_{23} (GPa)	G_{13} (GPa)
42.50	42.50	7.61	0.2177	0.2429	0.2429	3.29	2.89	2.89

Once the homogenized material properties were obtained, modeling of CFC parts in Ansys was very similar to the PMMA parts. In fact, with the exception of notch diameter and thickness, P1 and the CFC parts share similar dimensions; therefore, loading and constraints were applied to the CFC parts in the same manner as P1. Additionally, the Fujifilm Prescale was unable to be used for model verification since the CFC parts were thin, and the pressure paper lacked resolution.

b. Ansys Composite PrepPost Model

In addition to the homogenized models, the Ansys Composite PrepPost (ACP) modules were also used to model the CFC parts. Unlike the homogenized model, ACP allows the user to create a laminate utilizing the material properties of the individual lamina. For example, once the material properties associated with the individual plies are input into Ansys's engineering data, the ACP (Pre) module can be used to orientate the plies, assign thicknesses to each of the plies, and create a stacking sequence for the laminate. Additionally, as shown in Figure 27, the fiber orientation, shown by the green arrows, of a unidirectional ply and the total thickness of the laminate can be verified prior to solving the model in the static structural module.

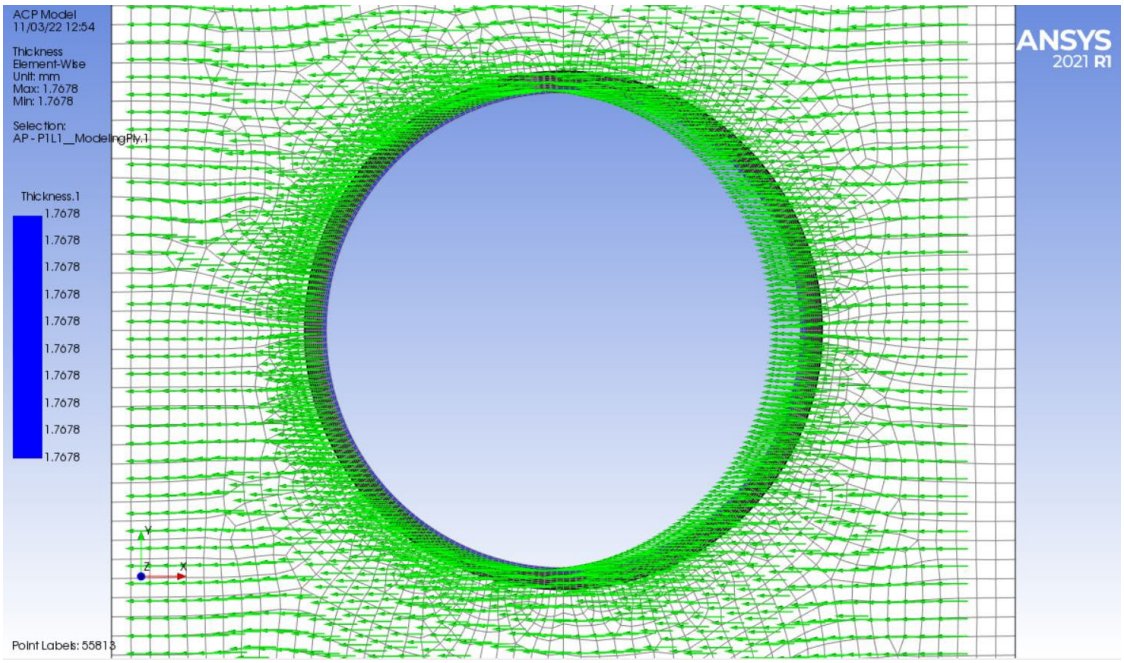

Figure 27. ACP (Pre) ply orientation and laminate thickness

As shown in Figure 28, the ACP (Pre) module is used to model the laminate; a mechanical module is used to model the bolt; a static structural module is used to solve the bolted joint model; and, unlike the previously discussed modeling techniques, the ACP (Post) module is used to investigate the results at the lamina or ply-wise level. As shown in Figure 29, the ACP (Post) module provides similar results as the static structural model; however, results are presented at the ply-wise level. In addition, many analyses specific to composite materials can be carried out in ACP (Post). Therefore, in addition to the homogenized models, an ACP model was generated for all CFC parts to determine whether or not there is a difference between the two numerical analyses.

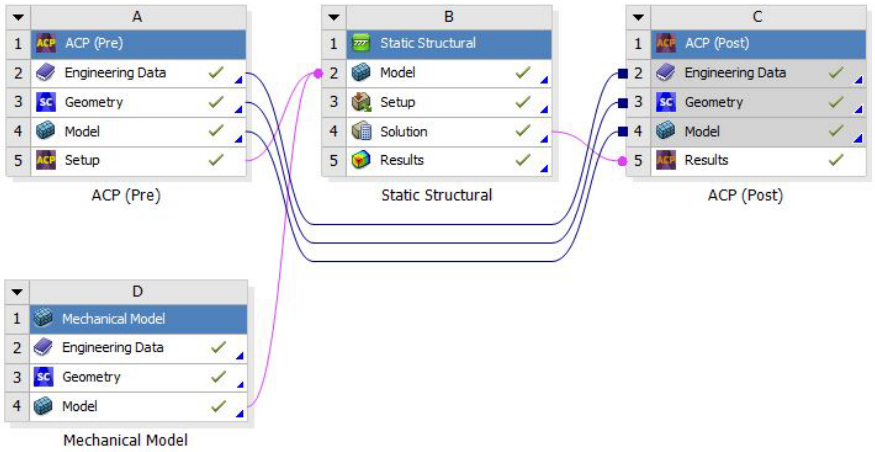

Figure 28. Ansys workbench using ACP modeling

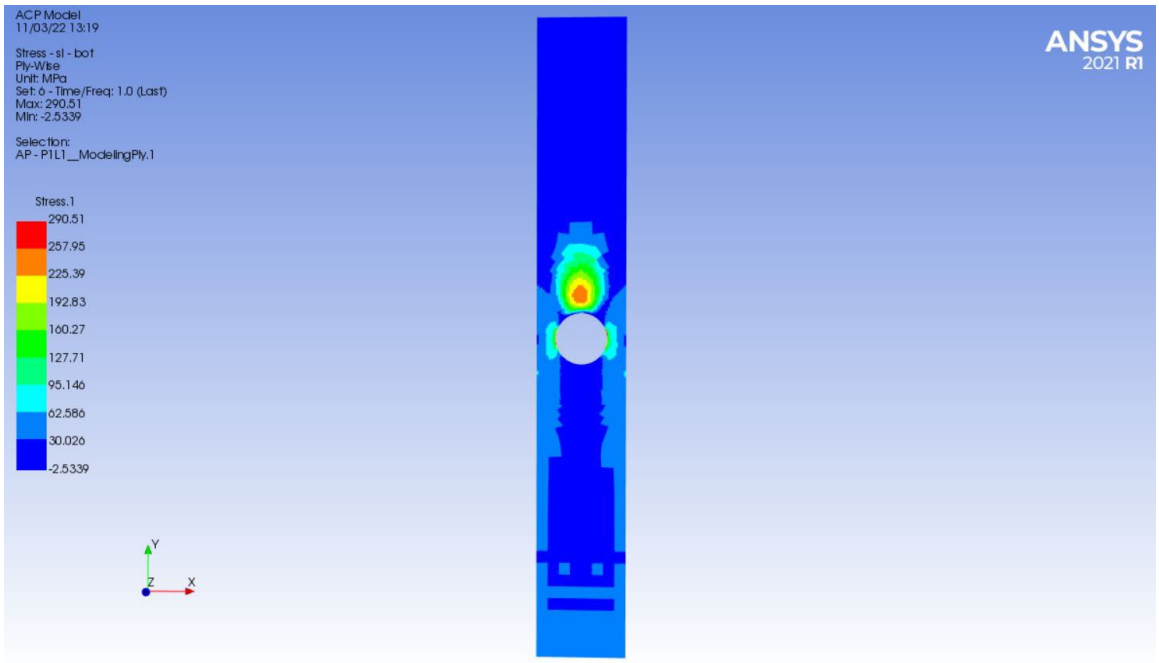

Figure 29. Ply-wise stress result in ACP (Post)

THIS PAGE INTENTIONALLY LEFT BLANK

IV. RESULTS AND DISCUSSION

A. PMMA

Simulated bolted joint loading of PMMA, using an INSTRON 5982 tensile test, provided important information needed to establish boundary conditions for the FEA models, namely, the failure force. In addition, the actual fracture results were necessary to validate the predictions obtained from Kwon's proposed failure criteria. As shown in Figures 30 through 32, parts P1, P2, and P3 experienced fracture similar to notched samples under uniaxial tensile loading. A quick visual inspection suggests that fracture initiates and propagates from the 90º position on the notch surface. Additionally, the difference in bolt diameters appears to have little effect on the site of fracture initiation and crack propagation direction. Therefore, parts P4, P5, and P6 were manufactured in order to obtain easily identifiable variation in the fracture initiation location and crack direction. As shown in Figures 33 and 34, unlike parts P1, P2, and P3, fracture is easily observed at a location other than the 90º position on the notch surface for all specimens. Additionally, there is a clear difference in the fracture initiation location and crack propagation path for the specimens loaded with the 8 mm bolt versus the 5 mm bolt.

Figure 30. Specimen fracture with 8 mm bolt: a) P1, b) P2, and c) P3

Figure 31. Specimen fracture with 6 mm bolt: a) P1, b) P2, and c) P3

Figure 32. Specimen fracture with 5 mm bolt: a) P1, b) P2, and c) P3

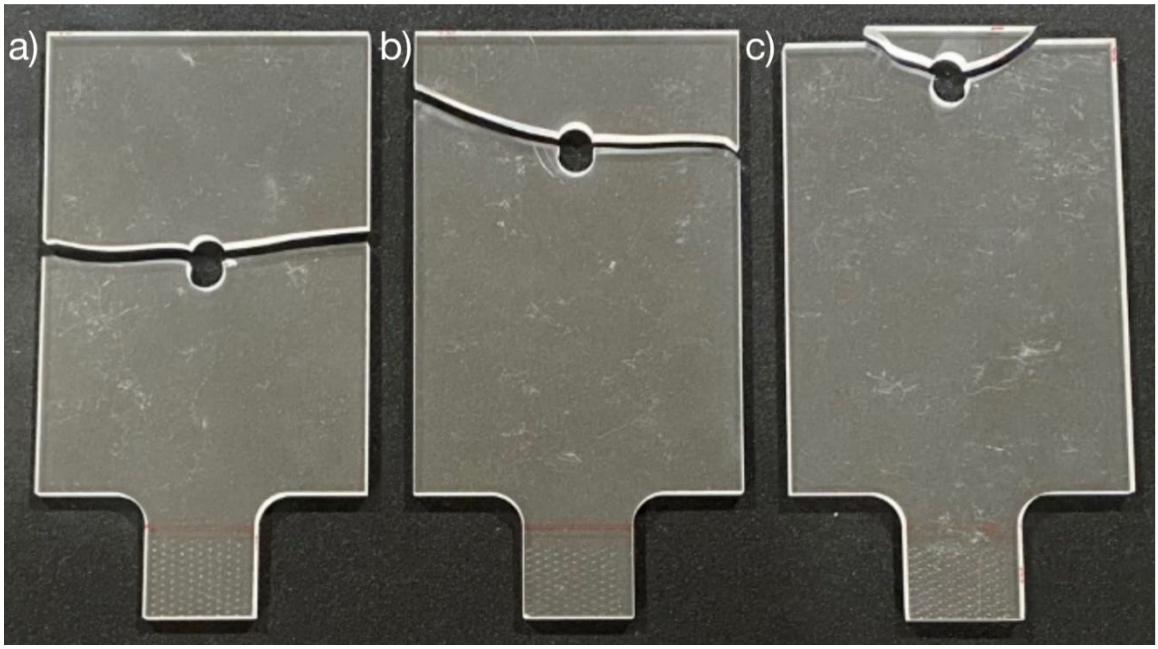

Figure 33. Specimen fracture with 8 mm bolt: a) P4, b) P5, and c) P6

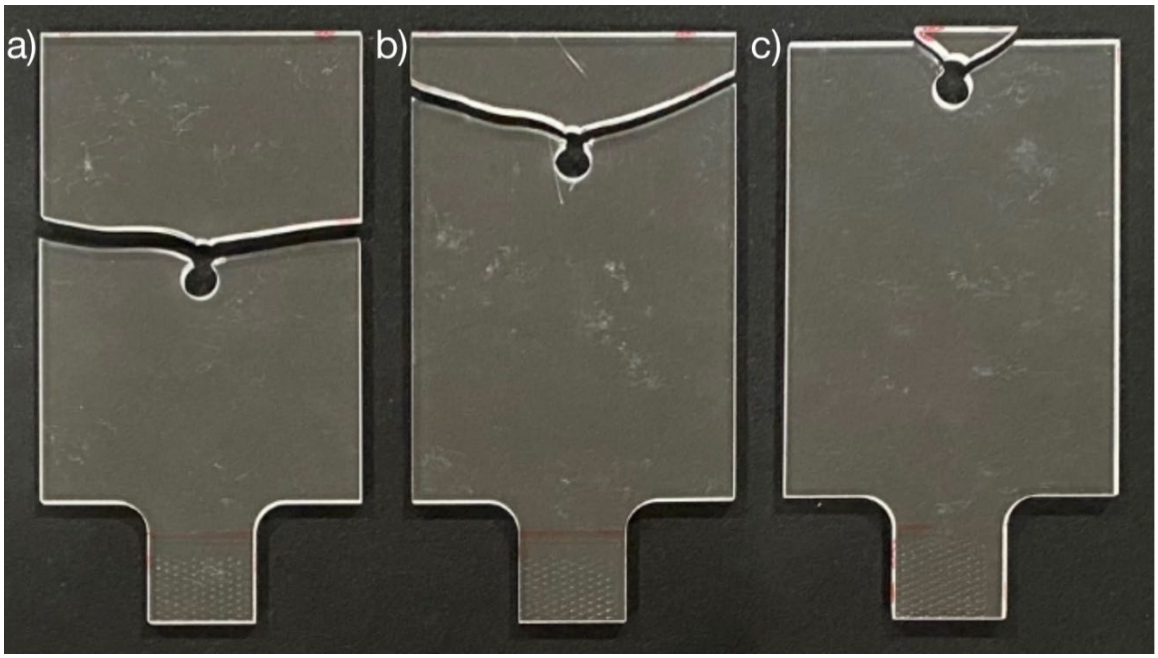

Figure 34. Specimen fracture with 5 mm bolt: a) P4, b) P5, and c) P6

Aside from the visual inspection, a more thorough quantitative analysis of the fracture initiation location and the crack path was conducted for all specimens using templates. Templates were used so that the fracture profiles could be traced, and approximate measurements could be taken. As shown in Figure 35, using a ruler and protractor, approximate fracture location and initial crack angle were determined with respect to the Y-axis. Table 7 provides the results of the analysis.

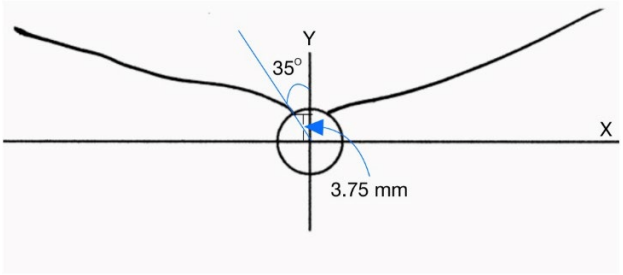

Figure 35. Template with fracture profile of P5 with 5 mm bolt (specimen 1)

Table 7. Experimental fracture location and angle

P1: w = 14 mm and e = 50 mm		
Nominal Bolt Diameter (mm)	Y - Coord. (mm)	Angle (º)
8	0.0	90
6	1.0	90
5	0.0	90
P2: w = 24 mm and e = 50 mm		
Nominal Bolt Diameter (mm)	Y - Coord. (mm)	Angle (º)
8	0.0 - 1.5	80 - 90
6	1.0	75
5	0.0	85
P3: w = 24 mm and e = 10 mm		
Nominal Bolt Diameter (mm)	Y - Coord. (mm)	Angle (º)
8	1.0 - 2.0	70 - 80
6	1.0	75
5	2.0	55
P4: w = 72 mm and e = 50 mm		
Nominal Bolt Diameter (mm)	Y - Coord. (mm)	Angle (º)
8	1.5 - 2.0	80
5	3.0 - 3.75	50
P5: w = 72 mm and e = 24.6 mm		
Nominal Bolt Diameter (mm)	Y - Coord. (mm)	Angle (º)
8	1.5 - 2.0	70
5	3.5 - 3.75	35
P6: w = 72 mm and e = 10 mm		
Nominal Bolt Diameter (mm)	Y - Coord. (mm)	Angle (º)
8	1.0 - 2.0	75
5	2.0 - 3.0	50

Data obtained from the tensile tests revealed that less force is required to fracture PMMA specimens when a smaller bolt diameter is utilized. As shown in Figure 36 and Table 8, it appears that the applied force is independent of bolt diameter for P1. However, it becomes readily apparent when reviewing the results for P2 through P6 that less force is required for a smaller bolt diameter. The discrepancy in P1 may be attributed to the small cross-sectional area adjacent to the notch which requires minimal loading to

fracture. The smaller amount of force required to fracture the material may make it more difficult to resolve the differences between the bolts. For the same applied force, the smaller contact area associated with a smaller bolt diameter induces much higher stresses in the material. Therefore, material failure occurs at reduced loading when the bolt diameter is decreased, or the clearance is increased.

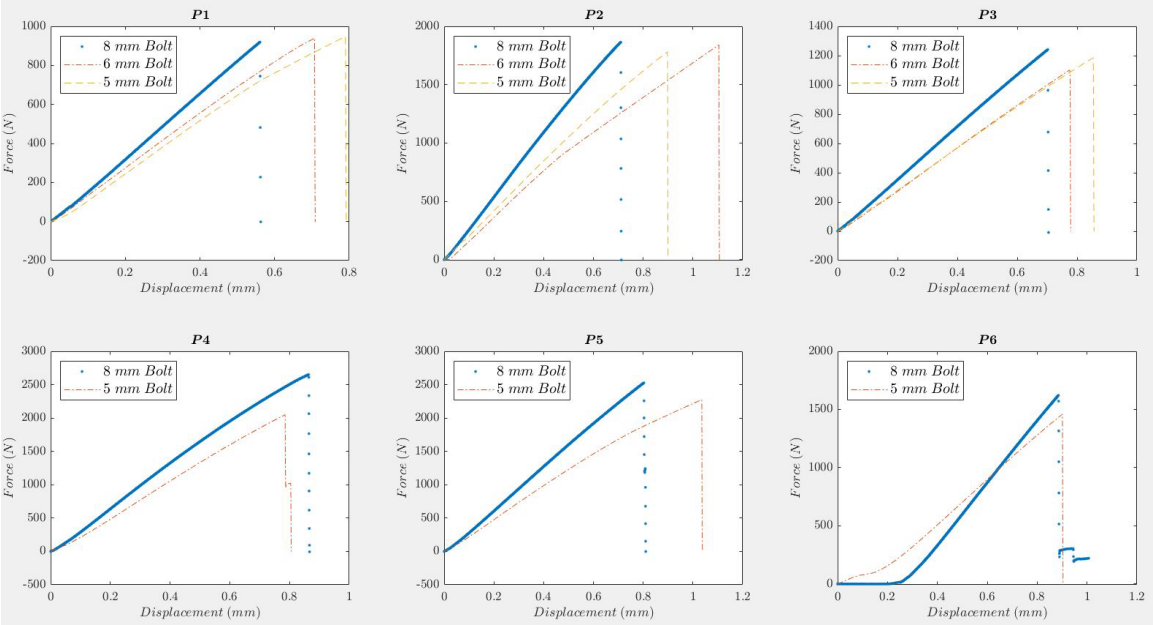

Figure 36. PMMA tensile test results

Table 8. PMMA tensile test results

P1: w = 14 mm and e = 50 mm		
Nominal Bolt Diameter (mm)	Displacement (mm)	Force (N)
8	0.57	878.6
6	0.71	939.0
5	0.79	947.7
P2: w = 24 mm and e = 50 mm		
Nominal Bolt Diameter (mm)	Displacement (mm)	Force (N)
8	0.74	1846.5
6	1.10	1841.9
5	0.90	1781.6
P3: w = 24 mm and e = 10 mm		
Nominal Bolt Diameter (mm)	Displacement (mm)	Force (N)
8	0.74	1222.5
6	0.78	1102.2
5	0.85	1186.2
P4: w = 72 mm and e = 50 mm		
Nominal Bolt Diameter (mm)	Displacement (mm)	Force (N)
8	0.70	2288.0
5	0.83	2185.5
P5: w = 72 mm and e = 24.6 mm		
Nominal Bolt Diameter (mm)	Displacement (mm)	Force (N)
8	0.79	2516.3
5	0.84	2019.0
P6: w = 72 mm and e = 10 mm		
Nominal Bolt Diameter (mm)	Displacement (mm)	Force (N)
8	0.71	1617.4
5	0.88	1553.3

As previously mentioned, loading results obtained from the tensile tests were used to establish the boundary conditions for the FEA models. Once the models were run, additional model validation was accomplished by analyzing the stress concentration factors (SCF) obtained from the model results. The SCF is given by

$$K = \frac{\sigma_{\max}}{\sigma_{nom}}, \tag{12}$$

where $\sigma_{\max}$ is the maximum stress, and σ_{nom} is the average stress associated with the plane that is perpendicular to applied loading and passes through the maximum stress. As shown in Figure 37, data has already been compiled and charts have been formulated to predict the SCF for flat bars loaded in tension by a pin. Utilizing curve A in Figure 37, the SCF associated with P1 is approximately 2.4 and the SCF associated with P2 and P3 is approximately 3.3. As shown in Table 9, P1 and P2 agree with the results obtained from Figure 37. The chart does not account for variations in pin size and the effects of boundary conditions. Therefore, slight variability in the results for P1 and P2 specimens may be attributed to the difference in bolt diameter, and the SCF of 5 for the P3 specimens may be a result of the notch being located near the boundary of the material. The d/D calculated for P4, P5, and P6 is 0.11. The intersection of 0.11 and curve A coincides with a point off the chart. However, the calculated SCFs for P4, P5, and P6 all exceed a value of 7, which trend in the correct direction.

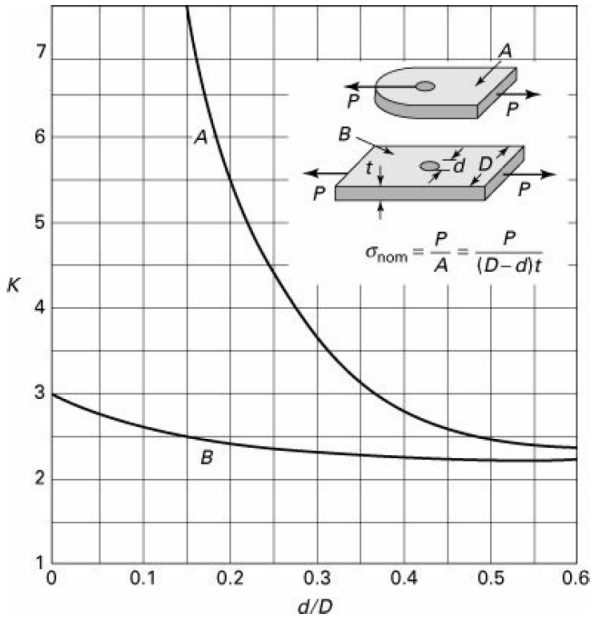

Figure 37. Stress concentration factor: A – for flat bar loaded in tension by a pin; B – for a flat bar in axial tension. Source: [13].

Table 9. PMMA stress concentration factors

P1: w = 14 mm and e = 50 mm					
Nominal Bolt Diameter (mm)	Force (N)*	Area (m^2)**	σ_{nom} (MPa)	σ_{max} (MPa)**	K
8	878.6	2.36E-05	37.2	86.2	2.3
6	939.0	2.37E-05	39.6	94.5	2.4
5	947.7	2.37E-05	39.9	95.6	2.4
P2: w = 24 mm and e = 50 mm					
Nominal Bolt Diameter (mm)	Force (N)*	Area (m^2)**	σ_{nom} (MPa)	σ_{max} (MPa)**	K
8	1846.5	6.64E-05	27.8	102.1	3.7
6	1841.9	6.50E-05	28.3	93.0	3.3
5	1781.6	6.42E-05	27.7	89.9	3.2
P3: w = 24 mm and e = 10 mm					
Nominal Bolt Diameter (mm)	Force (N)*	Area (m^2)**	σ_{nom} (MPa)	σ_{max} (MPa)**	K
8	1222.5	6.64E-05	18.4	92.3	5.0
6	1102.2	6.52E-05	16.9	84.2	5.0
5	1186.2	6.52E-05	18.2	91.1	5.0
P4: w = 72 mm and e = 50 mm					
Nominal Bolt Diameter (mm)	Force (N)*	Area (m^2)**	σ_{nom} (MPa)	σ_{max} (MPa)**	K
8	2288.0	2.58E-04	8.9	101.6	11.5
5	2185.5	2.75E-04	8.0	101.4	12.8
P5: w = 72 mm and e = 24.6 mm					
Nominal Bolt Diameter (mm)	Force (N)*	Area (m^2)**	σ_{nom} (MPa)	σ_{max} (MPa)**	K
8	2516.3	2.58E-04	9.7	120.2	12.3
5	2019.0	2.78E-04	7.3	95.4	13.1
P6: w = 72 mm and e = 10 mm					
Nominal Bolt Diameter (mm)	Force (N)*	Area (m^2)**	σ_{nom} (MPa)	σ_{max} (MPa)**	K
8	1617.4	2.58E-04	6.3	107.9	17.2
5	1553.3	2.62E-04	5.9	106.4	17.9

* Obtained from tensile test results.

** Calculated or obtained from FEA results.

Once the models appeared to be fully validated, stress gradients at the location of fracture initiation were calculated. Algebraic manipulation of Equation (10) yields

$$\sigma_1 \geq \left(\left| \frac{\sigma_1}{ds} \right| \overline{\kappa}_{fail} \right)^{\frac{1}{3}}, \tag{13}$$

where $\overline{\kappa}_{fail}$ is equal to $2E\kappa_{fail}$, which, as previously mentioned, is assumed to be a material constant. Prior research provided a $\overline{\kappa}_{fail}$ value of 408 MPa^{2}m. Therefore, only the stress gradient was needed to apply Kwon's failure criteria and predict the local failure stress. First, in addition to the failure angle determined from experimental results, stress gradients were calculated at approximately 45 degrees above and below the actual fracture angle. As discussed in [6], the failure path of a brittle material appeared to coincide with the shallowest gradient emanating from the location of fracture initiation. However, contrary to [6], examination of the stress gradient results suggest that the failure path coincides with a steeper gradient. In fact, in most cases, the initial fracture direction coincides with the steepest gradient. Once the calculated stress gradients were obtained, the stress gradients and the previously mentioned $\overline{\kappa}_{fail}$ value were input into Equation (13). Unfortunately, the results proved to be inconclusive. The resulting local failure stresses varied considerably. In some cases, the local failure stress failed to meet the first criterion for all three gradients emanating from the site of fracture initiation. In other instances, both criteria were satisfied by all three gradients. The PMMA used to fabricate the specimens was from a different manufacturer than the specimens used to determine $\overline{\kappa}_{fail}$. Therefore, the erroneous results were initially attributed to the variability of PMMA produced by the different manufacturers. However, as seen in Table 10, even with an assumed $\overline{\kappa}_{fail}$ value of 800 MPa^{2}m, percent error associated with the proposed failure criteria ranges from -27.7 % to 38.6 %. In addition, error tends to increase as bolt diameter is decreased. Due to the discrepancies in the failure predictions, further examination of the FEA models and fracture specimens was conducted to determine if there were any underlying similarities which may not be accounted for in the currently proposed failure criteria.

Table 10. Failure stress prediction ($\bar{\kappa}_{fail}$ = 800 MPa^{2}m)

P1: w = 14 mm and e = 50 mm					
Nominal Bolt Diameter (mm)	$\sigma_{l\ (Model)}^{*}$ (MPa)	Normalized Gradient (MPa/m)	$\bar{\kappa}_{fail}$ (MPa^{2}m)	$\sigma_{l\ (Theory)}$ (MPa)	Error (%)
8	86.2	-673.5	800	81.4	-5.6
6	94.5	-704.9	800	82.6	-12.6
5	95.6	-704.6	800	82.6	-13.6
P2: w = 24 mm and e = 50 mm					
Nominal Bolt Diameter (mm)	$\sigma_{l\ (Model)}^{*}$ (MPa)	Normalized Gradient (MPa/m)	$\bar{\kappa}_{fail}$ (MPa^{2}m)	$\sigma_{l\ (Theory)}$ (MPa)	Error (%)
8	102.1	-1117.1	800	96.3	-5.6
6	93.0	-517.5	800	74.5	-19.9
5	89.9	-514.0	800	74.4	-17.2
P3: w = 24 mm and e = 10 mm					
Nominal Bolt Diameter (mm)	$\sigma_{l\ (Model)}^{*}$ (MPa)	Normalized Gradient (MPa/m)	$\bar{\kappa}_{fail}$ (MPa^{2}m)	$\sigma_{l\ (Theory)}$ (MPa)	Error (%)
8	92.3	-1061.4	800	94.7	2.6
6	84.2	-554.3	800	76.3	-9.4
5	91.1	-551.3	800	76.1	-16.4
P4: w = 72 mm and e = 50 mm					
Nominal Bolt Diameter (mm)	$\sigma_{l\ (Model)}^{*}$ (MPa)	Normalized Gradient (MPa/m)	$\bar{\kappa}_{fail}$ (MPa^{2}m)	$\sigma_{l\ (Theory)}$ (MPa)	Error (%)
8	101.6	-1180.0	800	98.1	-3.4
5	101.4	-2035.1	800	117.6	16.0
P5: w = 72 mm and e = 24.6 mm					
Nominal Bolt Diameter (mm)	$\sigma_{l\ (Model)}^{*}$ (MPa)	Normalized Gradient (MPa/m)	$\bar{\kappa}_{fail}$ (MPa^{2}m)	$\sigma_{l\ (Theory)}$ (MPa)	Error (%)
8	120.2	-1232.1	800	99.5	-17.2
5	95.4	-2893.9	800	132.3	38.6
P6: w = 72 mm and e = 10 mm					
Nominal Bolt Diameter (mm)	$\sigma_{l\ (Model)}^{*}$ (MPa)	Normalized Gradient (MPa/m)	$\bar{\kappa}_{fail}$ (MPa^{2}m)	$\sigma_{l\ (Theory)}$ (MPa)	Error (%)
8	107.9	-891.7	800	89.4	-17.2
5	106.4	-568.9	800	76.9	-27.7

* Maximum principal stress.

The first noticeable similarity between the models and the experimental results is that failure occurred at the maximum normal stress. Essentially, the site of fracture initiation coincided with the location of the global maximum principal stress in the model. As shown in Table 11, the location of maximum principal stress in the model agrees very well with the fracture initiation location in the specimens. A few items may account for the minimal discrepancy between the model and the experimental values: specimen and adapter were not vertically aligned and centered in the INSTRON 5982, potential flaws in the material, and loss of accuracy due to the method of measurement used for the experimental specimens. However, even without considering potential errors, the data strongly suggests that the maximum principal stress coincides with the site of initial material failure.

Table 11. Maximum principal stress in FEA versus experimental fracture initiation location

P1: w = 14 mm and e = 50 mm			
	FEA Model		Experimental
Nominal Bolt Diameter (mm)	Max Principal Stress (MPa)	Y - Coord. (mm)	Y - Coord. (mm)
8	86.2	0.0	0.0
6	94.5	0.4	1.0
5	95.6	0.4	0.0
P2: w = 24 mm and e = 50 mm			
	FEA Model		Experimental
Nominal Bolt Diameter (mm)	Max Principal Stress (MPa)	Y - Coord. (mm)	Y - Coord. (mm)
8	102.1	1.6	0.0 - 1.5
6	93.0	1.2	1.0
5	89.9	0.8	0.0
P3: w = 24 mm and e = 10 mm			
	FEA Model		Experimental
Nominal Bolt Diameter (mm)	Max Principal Stress (MPa)	Y - Coord. (mm)	Y - Coord. (mm)
8	92.3	1.6	1.0 - 2.0
6	84.2	1.3	1.0
5	91.1	1.3	2.0
P4: w = 72 mm and e = 50 mm			
	FEA Model		Experimental
Nominal Bolt Diameter (mm)	Max Principal Stress (MPa)	Y - Coord. (mm)	Y - Coord. (mm)
8	101.6	1.6	1.5 - 2.0
5	101.4	3.7	3.0 - 3.75
P5: w = 72 mm and e = 24.6 mm			
	FEA Model		Experimental
Nominal Bolt Diameter (mm)	Max Principal Stress (MPa)	Y - Coord. (mm)	Y - Coord. (mm)
8	120.2	1.6	1.5 - 2.0
5	95.4	3.9	3.5 - 3.75
P6: w = 72 mm and e = 10 mm			
	FEA Model		Experimental
Nominal Bolt Diameter (mm)	Max Principal Stress (MPa)	Y - Coord. (mm)	Y - Coord. (mm)
8	107.9	1.6	1.0 - 2.0
5	106.4	2.4	2.0 - 3.0

Once it was determined that the maximum principal stress coincides with the failure initiation location, various stresses and their associated gradients were analyzed in

the hope of finding a correlation to the initial fracture direction. Fortunately, as seen by comparing the initial fracture path in P5 in Figure 34 to the minimum principal stress contours in Figure 38, the minimum principal stress contours in the model closely resemble the initial fracture path in the specimen. The same correlation was observed in the other models and specimens. Therefore, realizing that the minimum principal stress is orientated 90º to the maximum principal stress, principal stress vectors were evaluated. As shown in Figures 39 through 42, using the vector principal stress solution in the static structural module, principal stress vectors at the maximum principal stress or material failure initiation location are easily obtained.

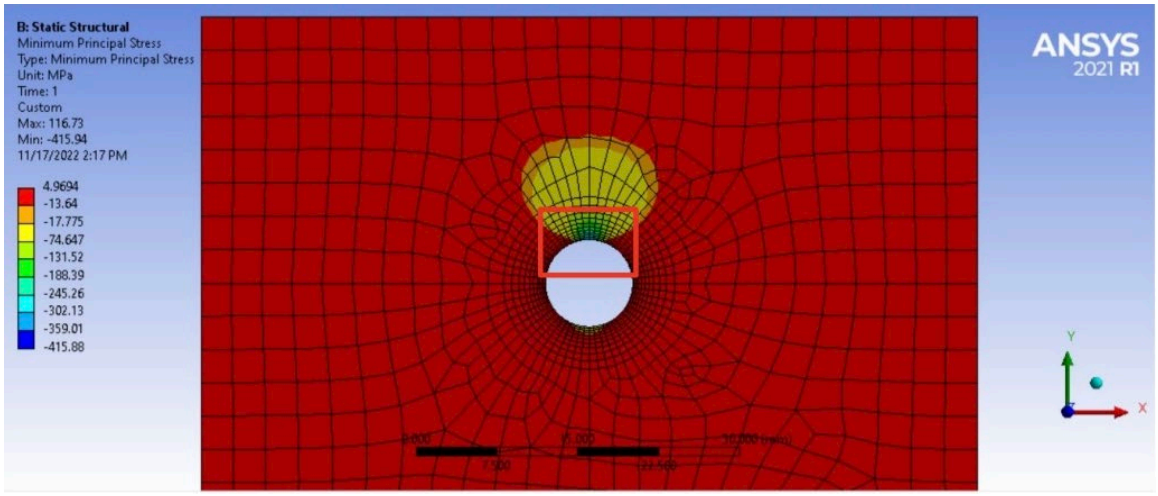

Figure 38. Minimum principal stress contours for P5 with 5 mm bolt

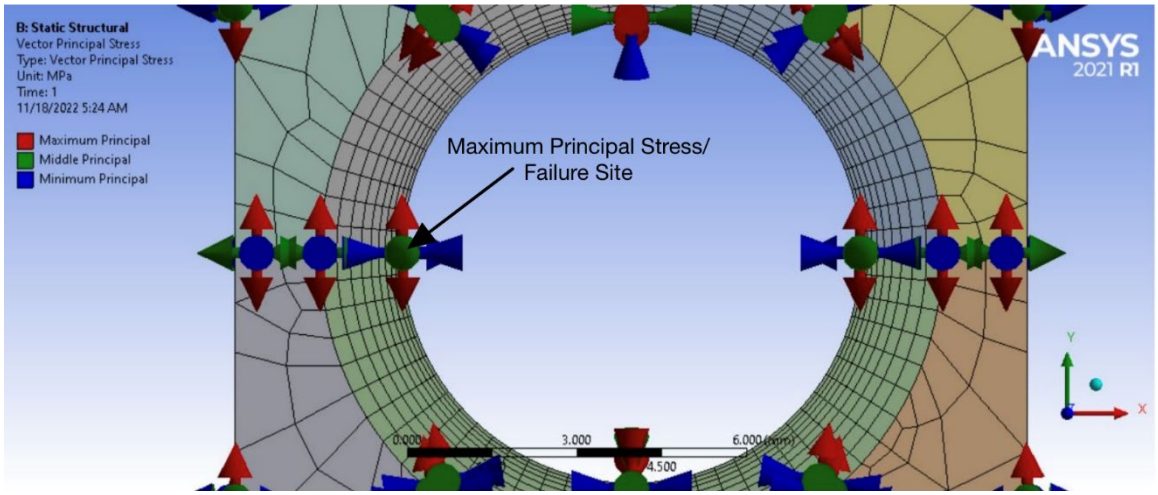

Figure 39. P1 with 8mm bolt vector principal stress model

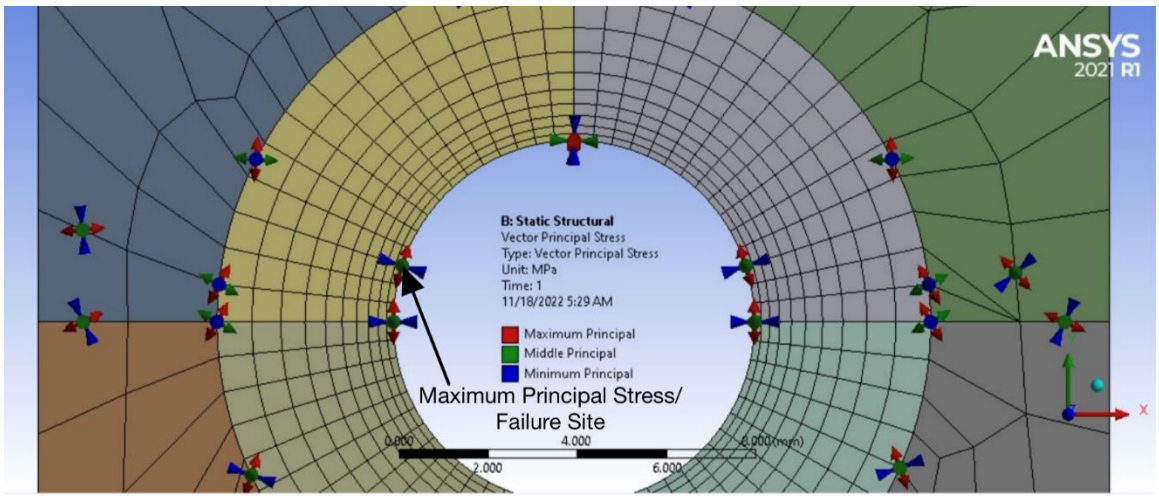

Figure 40. P3 with 5mm bolt vector principal stress model

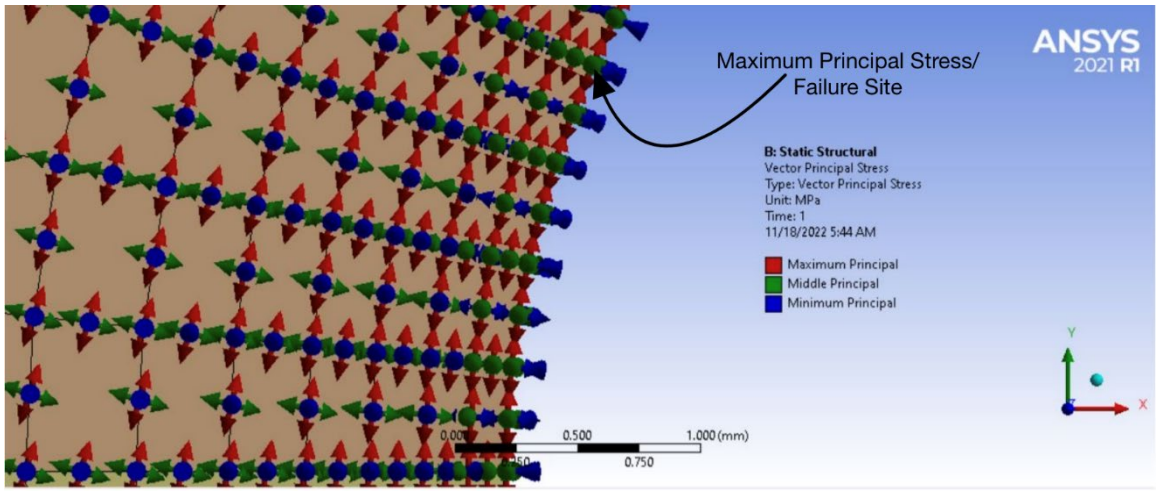

Figure 41. P4 with 8 mm bolt vector principal stress model

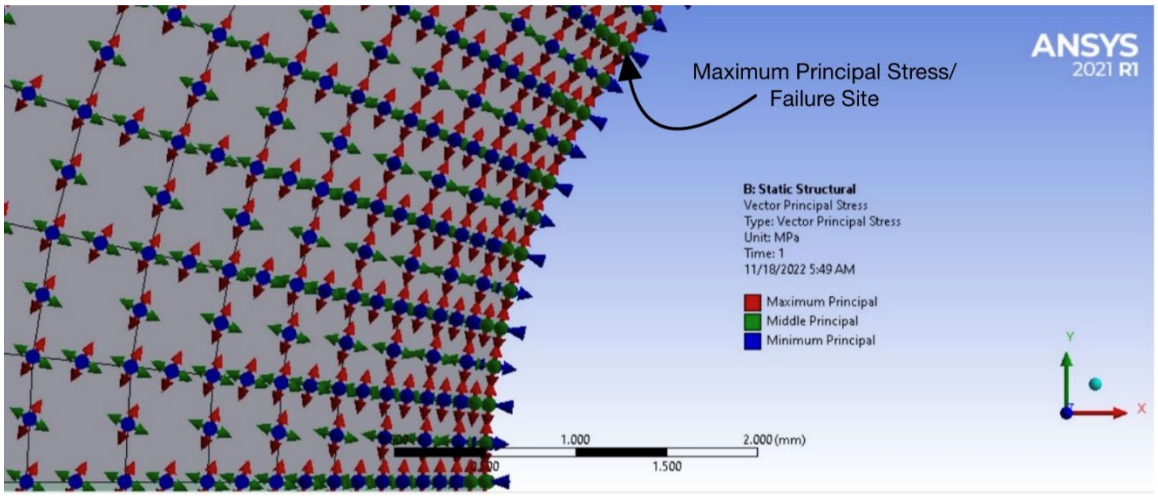

Figure 42. P6 with 5 mm bolt vector principal stress model

Principal stress vectors at the maximum principal stress or initial failure site were obtained for all models. Next, the angle perpendicular to the maximum principal stress vector, which coincides with the middle and minimum principal plane, was determined. As shown in Table 12, the angle perpendicular to the maximum principal stress vector closely resembles the experimental result. Therefore, in addition to material failure initiating at the location of the maximum principal stress, the data suggests that the initial fracture direction will be normal to the maximum principal stress vector at the maximum principal stress location.

Table 12. Angle perpendicular to maximum principal stress vector versus experimental angle

P1: w = 14 mm and e = 50 mm		
	FEA Model	Experimental
Nominal Bolt Diameter (mm)	Angle (º)	Angle (º)
8	90	90
6	85	90
5	85	90
P2: w = 24 mm and e = 50 mm		
	FEA Model	Experimental
Nominal Bolt Diameter (mm)	Angle (º)	Angle (º)
8	65	80 - 90
6	75	75
5	80	85
P3: w = 24 mm and e = 10 mm		
	FEA Model	Experimental
Nominal Bolt Diameter (mm)	Angle (º)	Angle (º)
8	65	70 - 80
6	70	75
5	70	55
P4: w = 72 mm and e = 50 mm		
	FEA Model	Experimental
Nominal Bolt Diameter (mm)	Angle (º)	Angle (º)
8	65	80
5	25	50
P5: w = 72 mm and e = 24.6 mm		
	FEA Model	Experimental
Nominal Bolt Diameter (mm)	Angle (º)	Angle (º)
8	65	70
5	20	35
P6: w = 72 mm and e = 10 mm		
	FEA Model	Experimental
Nominal Bolt Diameter (mm)	Angle (º)	Angle (º)
8	65	75
5	55	50

Utilizing the FEA model angles in Table 12, gradients were recalculated. As expected, there was negligible deviation between the previously calculated gradients and the newly calculated gradients because the newly proposed location and angle essentially mirrored the experimental results. Therefore, as seen in Table 10, local failure stress calculations were performed using the newly proposed failure initiation location and initial fracture direction. Additionally, Figures 43 through 48 are provided to further illustrate that the gradient associated with the initial fracture angle coincides with the steepest gradient in most cases.

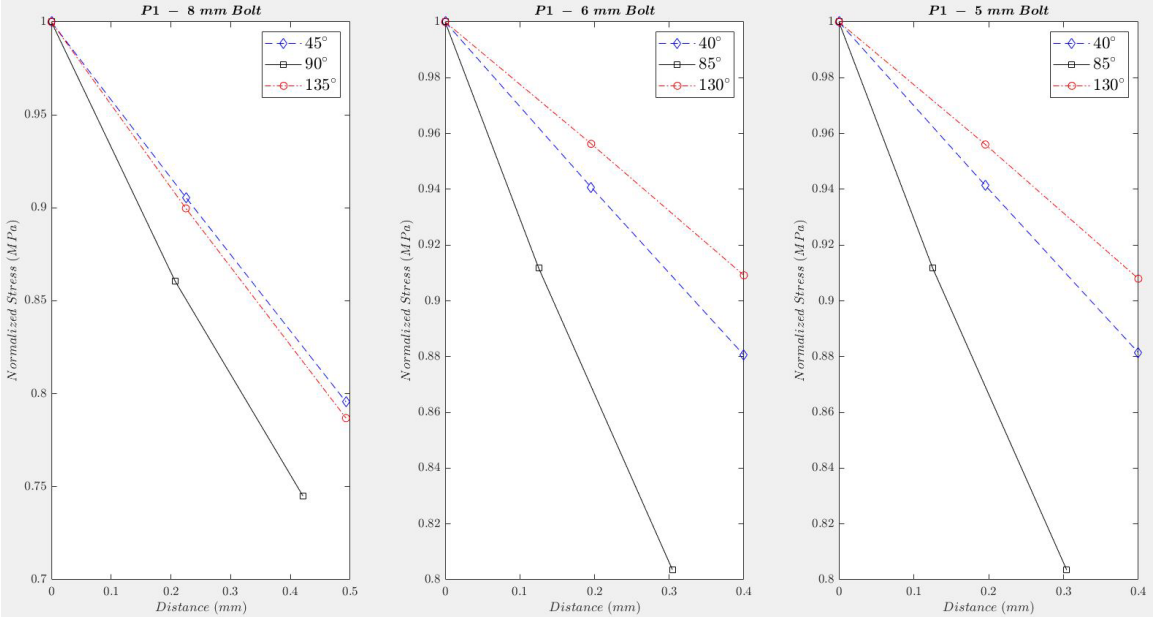

Figure 43. P1 gradients

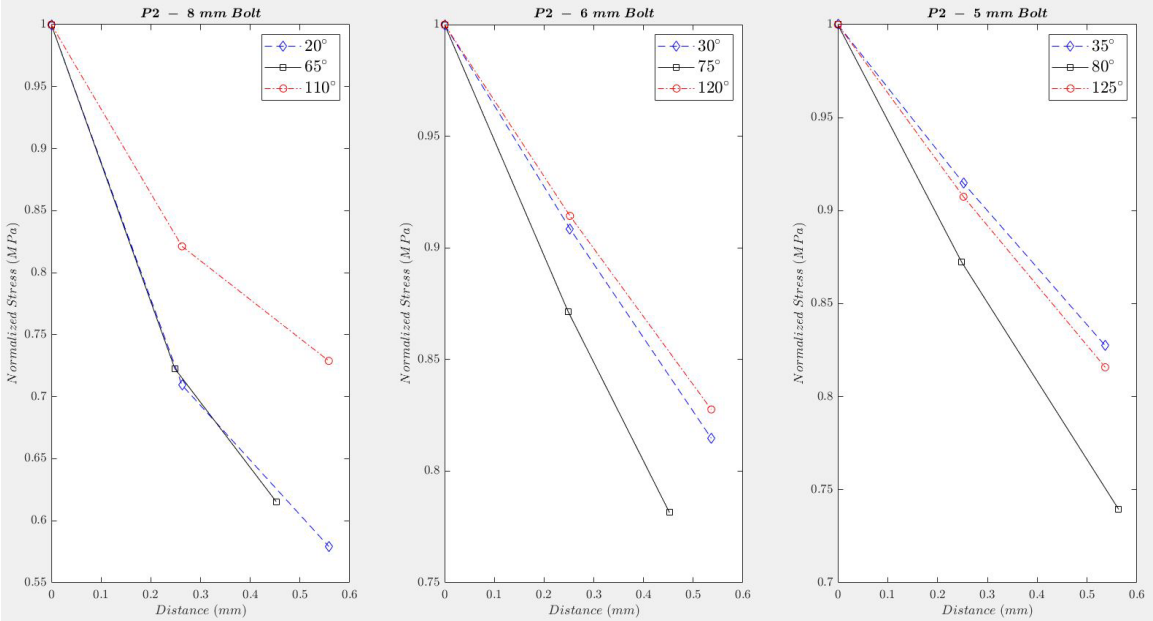

Figure 44. P2 gradients

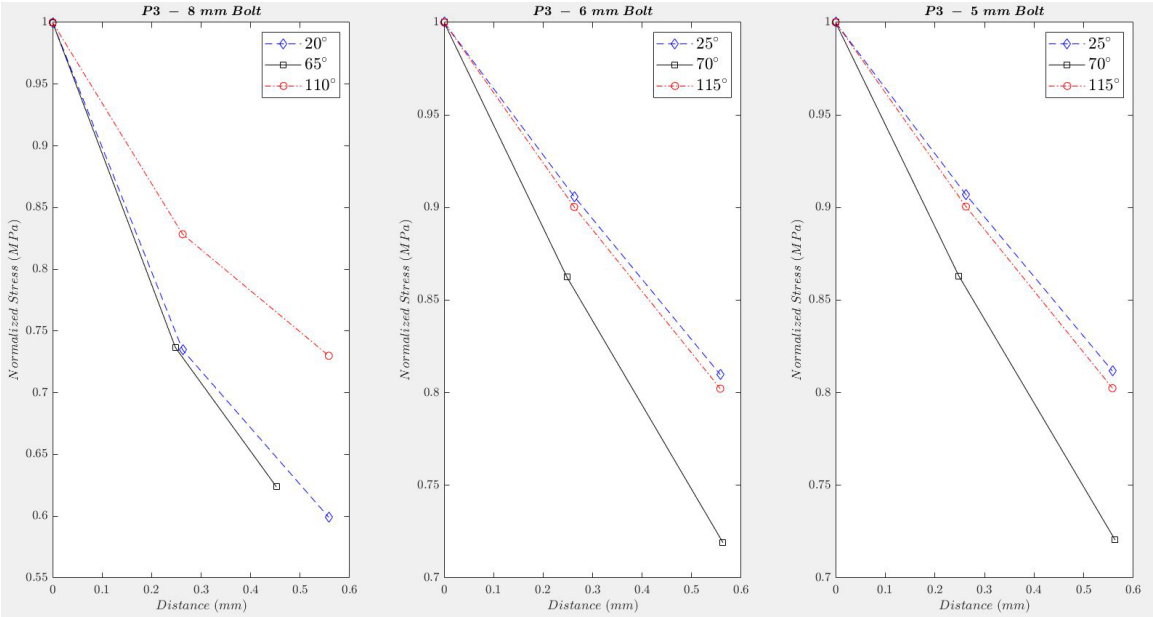

Figure 45. P3 gradients

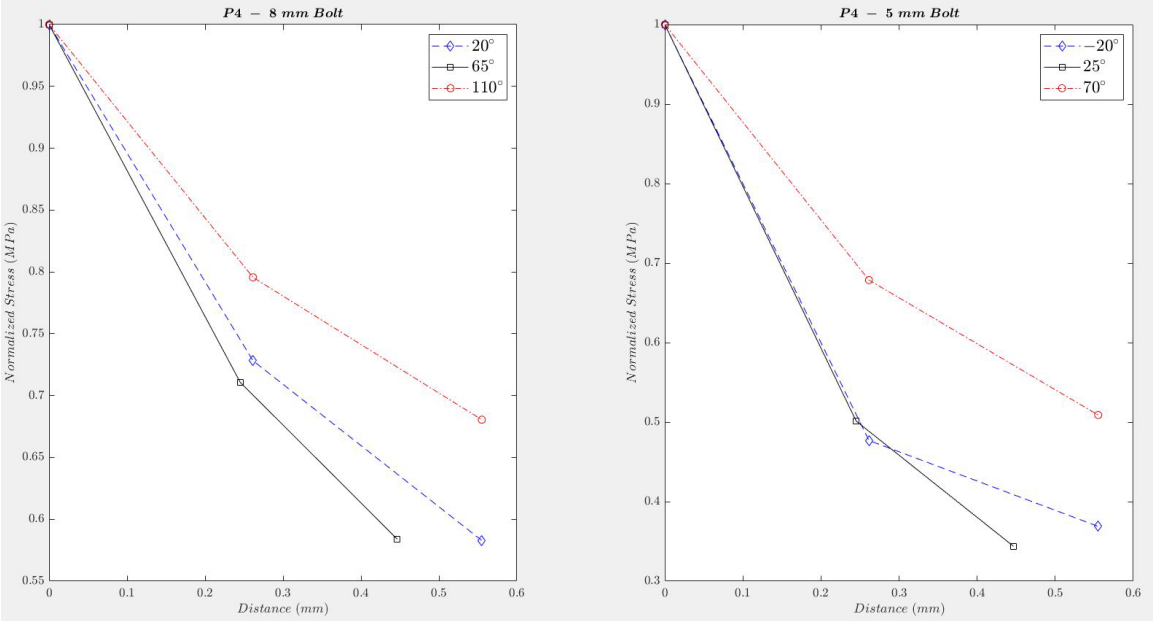

Figure 46. P4 gradients

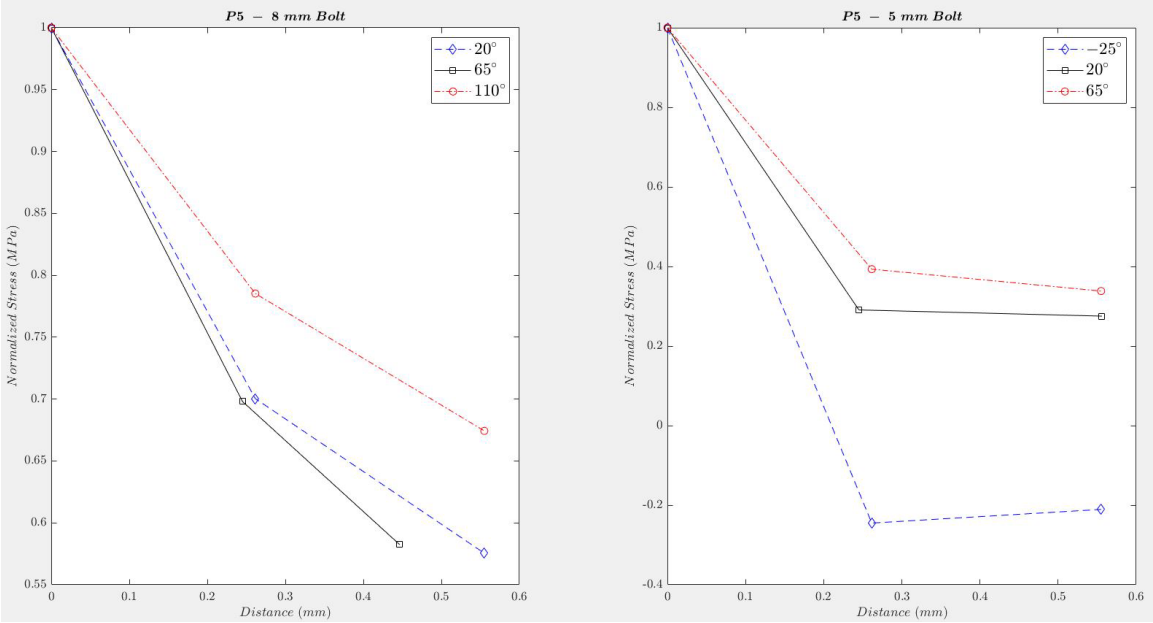

Figure 47. P5 gradients

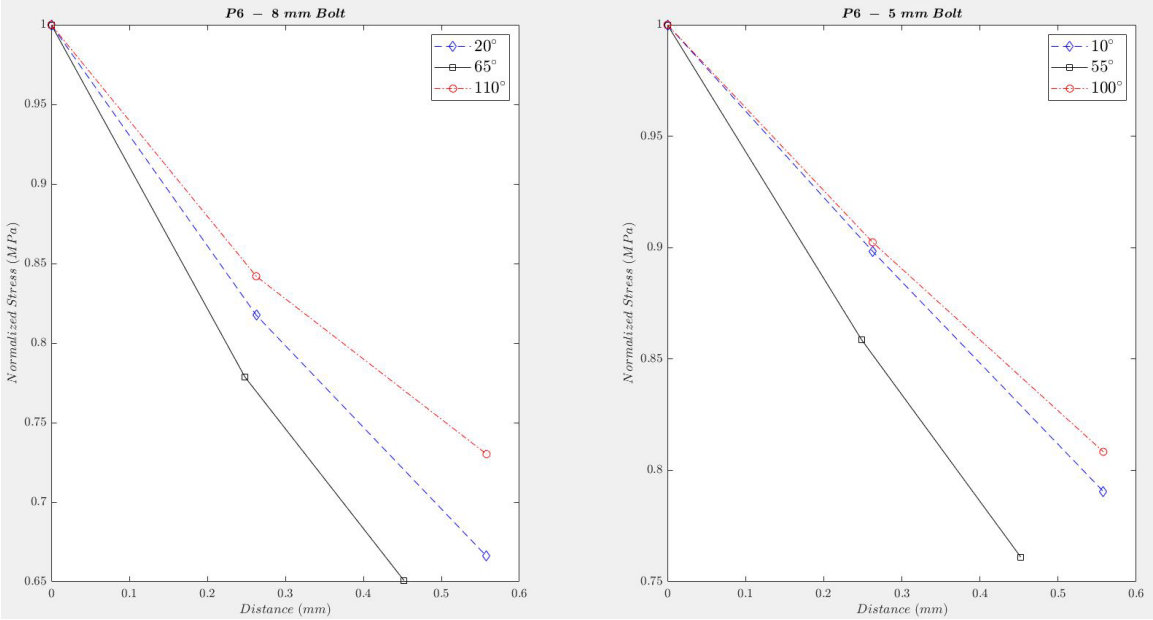

Figure 48. P6 gradients

Unfortunately, as of now, there does not appear to be a correlation between the normalized gradient and the local failure stress. As provided in [2], the yield strength of PMMA ranges from 53.8 MPa to 73.1 MPa. As seen in Table 11, the maximum principal stress satisfies the first criterion in Kwon's theory. However, the prediction of that stress, which is associated with the normalized gradient and Kwon's second criterion, needs further refinement to reduce the error associated with the predictions given by the current criteria.

B. CFC

Similar to the previous discussion of PMMA, the failure forces obtained from CFC tensile tests were utilized in the establishment of boundary conditions for the FEA models. In addition, the experimental tests were conducted to assess the accuracy and validity of Kwon's proposed failure criteria. As mentioned, for the purposes of this study, failure of the material was designated as the point of initial reduction in strength during tensile tests. However, tensile testing was allowed to progress further than the initial reduction in strength for one specimen (specimen 3) in an attempt to completely fracture the material. As shown in Figures 49 through 52, initial failure of the material

corresponds to the bearing failure mode. Failure of the material appears to be isolated to the contact area between the bolt and the composite. There was noticeable brooming or out of plane spreading of the laminate at the contact area in all instances. Therefore, the onset of delamination and matrix cracking was also visible with the naked eye. For the specimens that were allowed to progress further than the prescribed failure point, all three failure modes were easily observed.

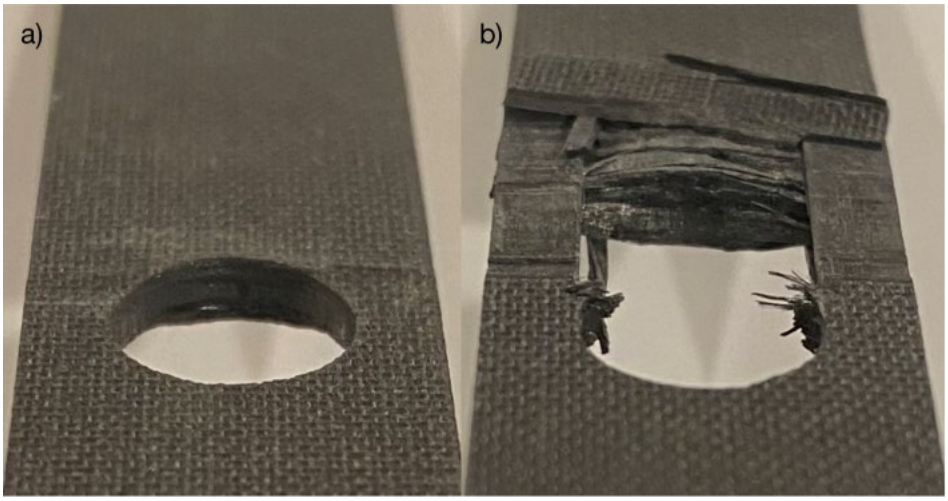

Figure 49. Failure results for C1: a) specimen 4 and b) specimen 3

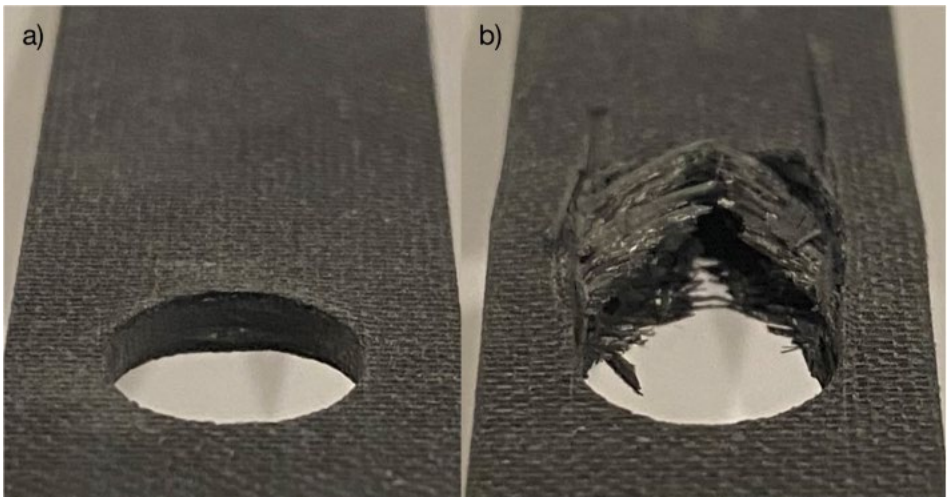

Figure 50. Failure results for C2: a) specimen 4 and b) specimen 3

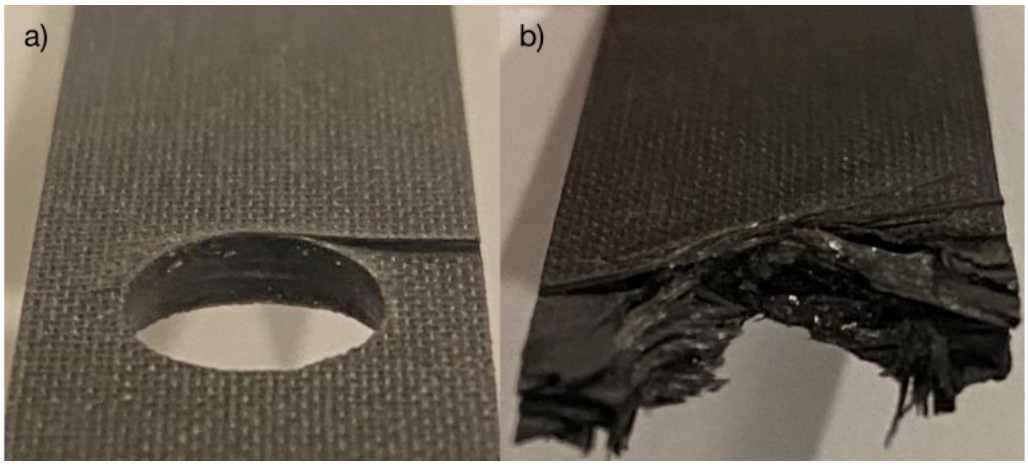

Figure 51. Failure results for Q1: a) specimen 4 and b) specimen 3

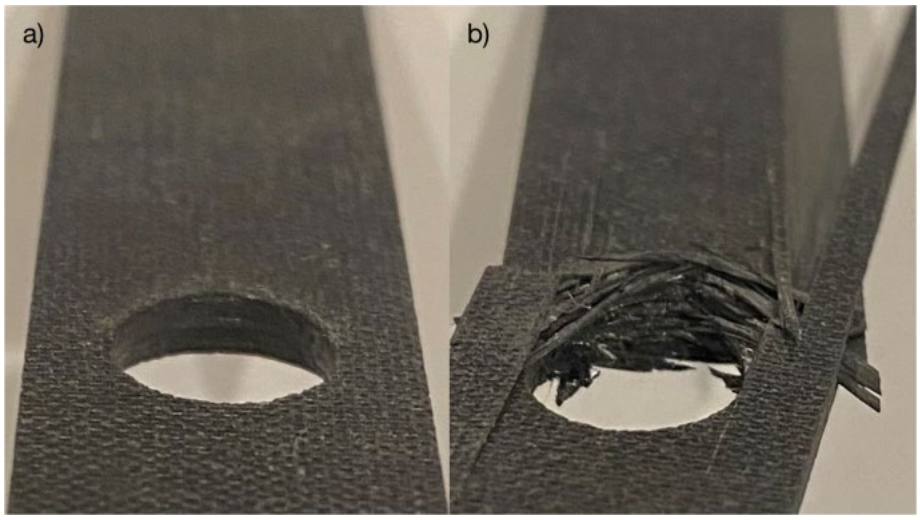

Figure 52. Failure results for Q2: a) specimen 4 and b) specimen 3

Following a visual inspection of the failed specimens, data obtained from the INSTRON 5982 tensile tests were compiled and reviewed. As shown in Figure 53 and Table 13, parts fabricated from the QI laminate were the strongest. The QI laminate, which has 4-fold rotational symmetry, resulted in the Q1 and Q2 parts having similar strengths. The C1 specimens withstood the least amount of force prior to failure. The higher strength in the QI parts may be attributed to the orientation of the carbon fiber filaments in relation to the applied load. Carbon fiber filaments are strongest when the load is applied parallel to the filament and buckling does not occur [2], [3]. Therefore,

due to the expected fanning load distribution induced in the material by the bolt, optimal load transfer occurs in the vertically and diagonally oriented plies. Lastly, even though the CP parts did not have the same strength as the QI parts, it is important to note that catastrophic failure did not occur in the specimens that were allowed to progress past initial failure.

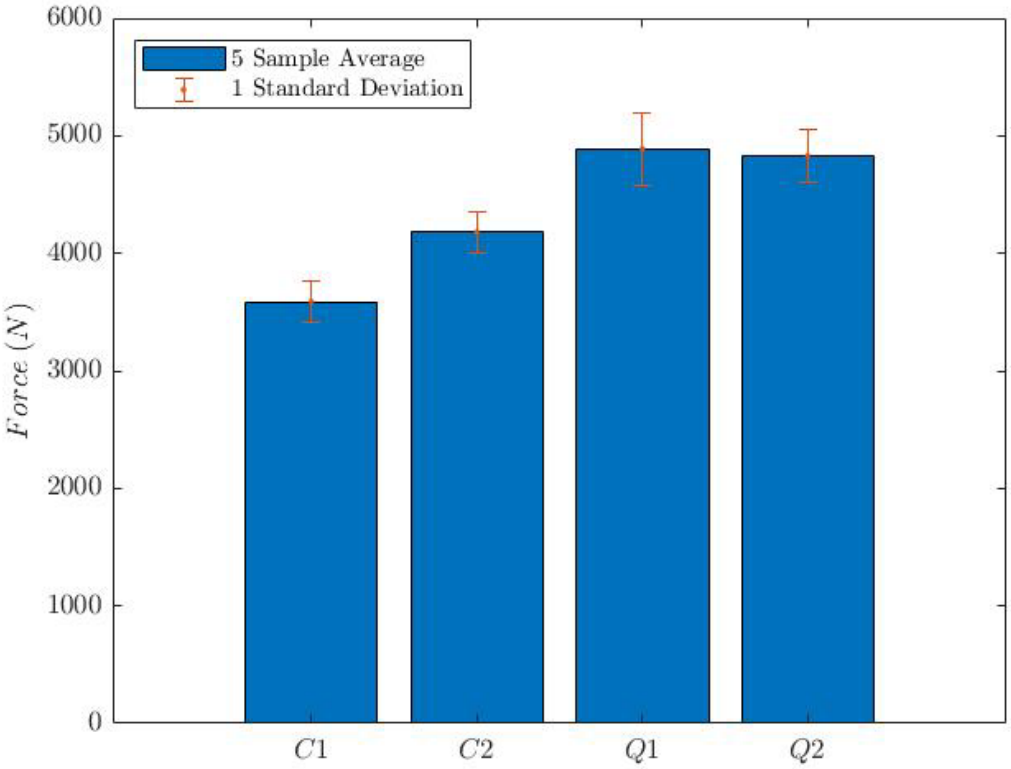

Figure 53. CFC tensile test results

Table 13. CFC tensile test results

C1: $[90/0/90]_s$	
Displacement (mm)	Force (N)
0.724	3588.4
C2: $[0/90/0]_s$	
Displacement (mm)	Force (N)
0.751	4178.4
Q1: $[90/0/45/-45/90/0]_s$	
Displacement (mm)	Force (N)
1.204	4887.3
Q2: $[0/90/-45/45/0/90]_s$	
Displacement (mm)	Force (N)
0.911	4829.2

The failure forces obtained from the tensile tests were applied to homogenized and ACP models. As expected, and shown in Figures 54 through 57, the smeared or homogenized models produced essentially uniform through thickness stress fields. On the other hand, the ACP models accounted for the variation in ply angle which resulted in an uneven load distribution amongst the plies. The ACP models further illustrate that the loading applied parallel to the carbon fiber filament is carried more efficiently. The higher maximum principal stresses, shown in red in Figures 54b through 57b, coincide with the 0º or vertical plies which are under tension at the location shown.

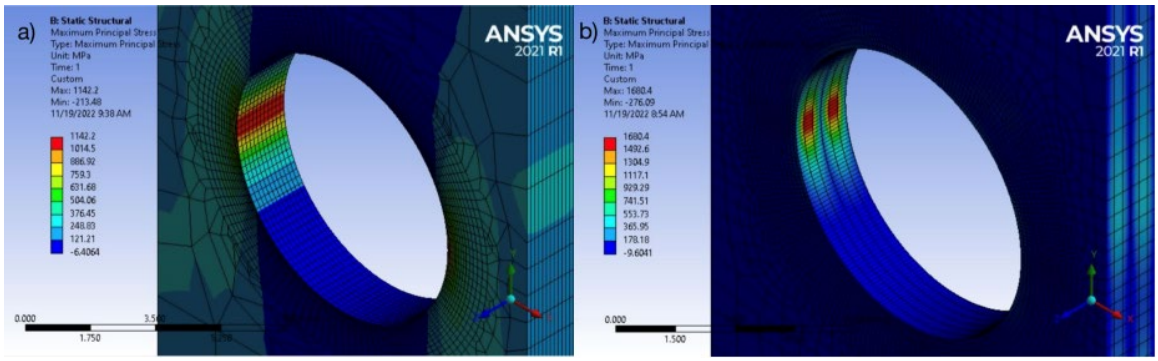

Figure 54. C1 Ansys models: a) homogenized and b) ACP

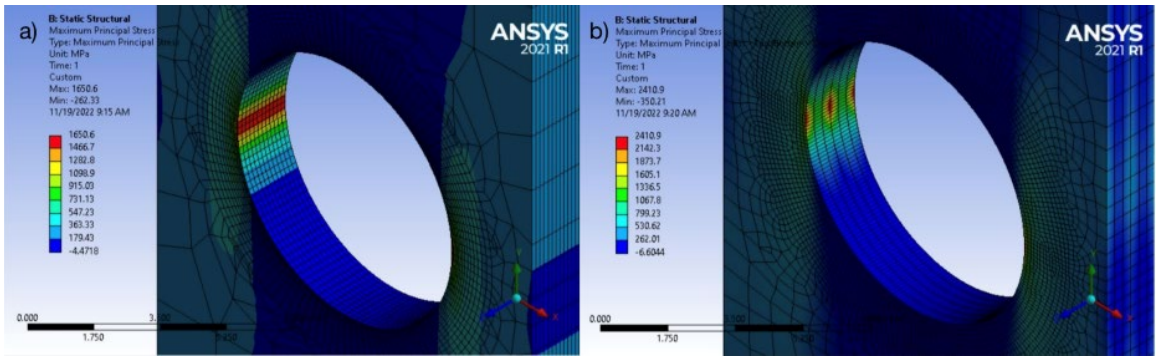

Figure 55. C2 Ansys models: a) homogenized and b) ACP

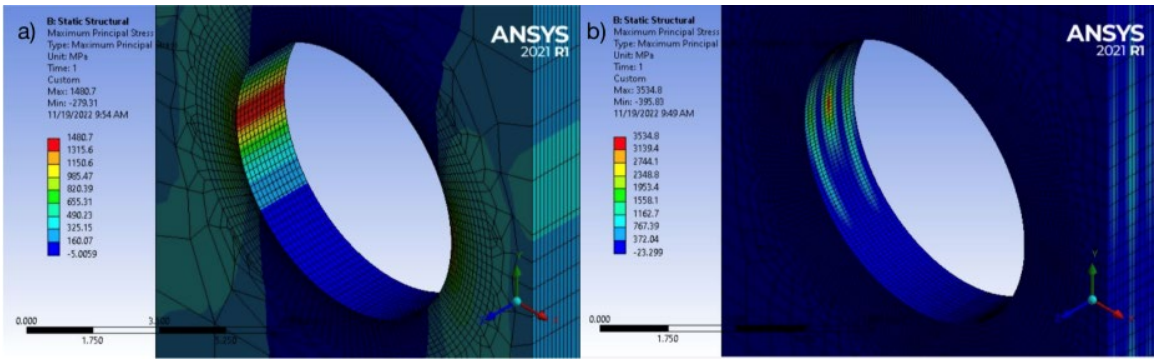

Figure 56. Q1 Ansys models: a) homogenized and b) ACP

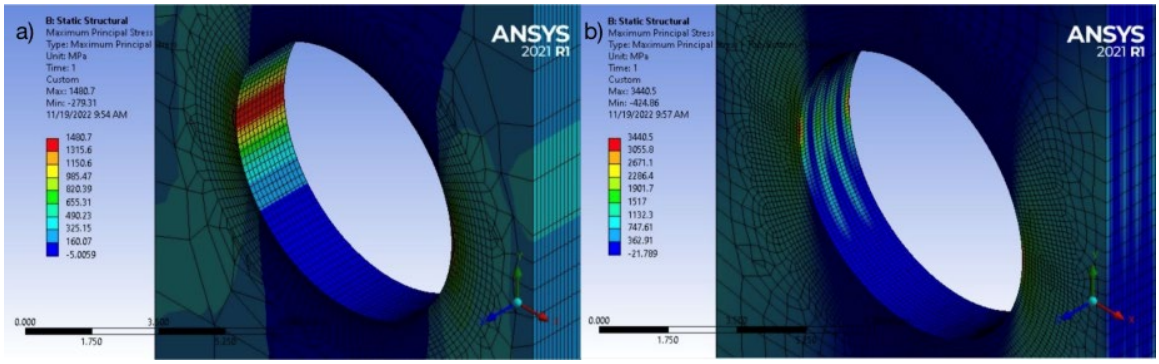

Figure 57. Q2 Ansys models: a) homogenized and b) ACP

Attempts were made to locate the exact site of failure initiation, however, due to multiple subcritical failure mechanisms associated with CFCs, cumulative damage occurred within the contact surface and no clear initiation point could be identified.

Knowing that failure occurred within the contact area of the bolt and composite, attempts were made to apply Kwon's failure criteria within the contact area.

Starting with the homogenized models, stresses within the contact area were assessed. Unfortunately, given the prescribed definition of Kwon's first criterion, stress magnitudes within the contact area were drastically lower than the failure stress obtained from standard tensile tests, and the first criterion was unable to be met. Similar results were obtained from an analysis of the ACP models. Potentially, at least for a macromechanical approach, the first criterion may need to be based on the most limiting subcritical failure mechanism. Due to an inability to identify the site of failure initiation and the lack of a failure stress for the first criterion, failure predictions could not be made with the proposed criteria in its current form. In addition, based on the results in the previous section, the criteria may need to be altered prior to implementation on quasi-brittle materials.

Although failure predictions were unable to be made with the currently proposed failure criteria, the two models, produced for the CFC analysis, revealed a vast difference in the modeling techniques. As shown in Table 14, there is an apparent difference between the two modeling techniques. The ACP models provide much higher stress results than the homogenized models. As previously discussed, the ACP model accounts for ply orientation, and therefore provides a better depiction of load distribution in the laminate. Once the appropriate adjustments are made to the currently proposed failure criteria, an ACP model should provide a better result for a macromechanical approach.

Table 14. Homogenized and ACP model stress comparison

C1: [90/0/90]$_s$						
	Homogenized			ACP		
Force* (N)	Max Principal (MPa)	Min Principal (MPa)	Max Shear (MPa)	Max Principal (MPa)	Min Principal (MPa)	Max Shear (MPa)
3588.4	1142.2	-378.7	571.8	1680.4	-546.7	846.5
C2: [0/90/0]$_s$						
	Homogenized			ACP		
Force* (N)	Max Principal (MPa)	Min Principal (MPa)	Max Shear (MPa)	Max Principal (MPa)	Min Principal (MPa)	Max Shear (MPa)
4178.4	1650.6	-468.7	825.8	2410.9	-600.2	1211.4
Q1: [90/0/45/-45/90/0]$_s$						
	Homogenized			ACP		
Force* (N)	Max Principal (MPa)	Min Principal (MPa)	Max Shear (MPa)	Max Principal (MPa)	Min Principal (MPa)	Max Shear (MPa)
4887.3	1480.7	-464.4	741.1	3534.8	-940.2	1775.3
Q2: [0/90/-45/45/0/90]$_s$						
	Homogenized			ACP		
Force* (N)	Max Principal (MPa)	Min Principal (MPa)	Max Shear (MPa)	Max Principal (MPa)	Min Principal (MPa)	Max Shear (MPa)
4829.2	1480.7	-464.4	741.1	3440.5	-965.7	1728.1

* Obtained from tensile test results.

In order to gain a better understanding of CFC subcritical failure mechanisms and provide information that may be useful for further research, a fractographic analysis was conducted on a sample of parts C1 and Q1 which were allowed to progress past the initial failure point. The fractographic analysis was conducted on the failed samples using a scanning electron and optical microscope.

First, the failed samples needed to be sectioned, so they could be viewed under the microscopes. C1 was sectioned along the red line in Figure 58. Additionally, all sections were cut to reduce their overall length, and special care was taken to ensure that the fracture surface was not disturbed.

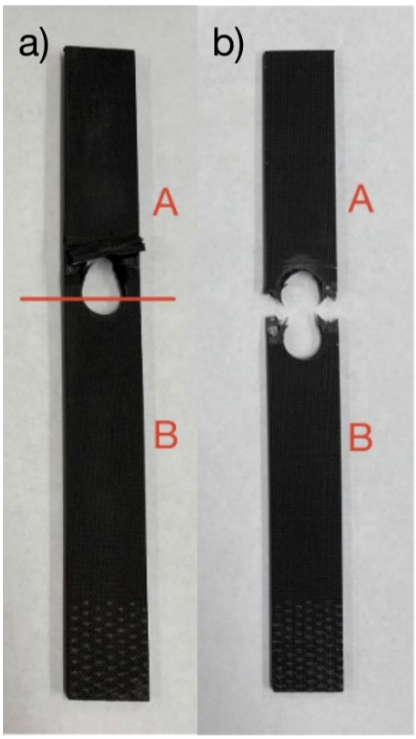

Figure 58. Section identification for fractographic analysis: a) C1 and b) Q1

The analysis began by viewing the fracture surface of section A, from the Q1 and C1 samples, in the scanning electron microscope (SEM). As shown in Figure 59, the failed material samples were oriented under the microscopes to obtain three different views of the fracture surface (Figure 59 is also provided as a reference when viewing the SEM and optical microscope images). As provided in Tables 2 and 3, and shown in Figure 60, ply thickness and orientation are very different between the CFC samples. The areas adjacent to the contact surface were under tension, and fiber failure is evident in the Q1 sample (Figure 60a). Unlike the Q1 sample, the 0º carbon fiber filaments adjacent to the contact surface remained intact in the C1 sample, and therefore had to be cut in order to view the failure surface. However, as seen in Figure 60b, the matrix is not as strong as the carbon fiber and failed under tensile loading. Following matrix failure, the 90º plies were pushed up through the composite. In addition, buckling delamination is clearly visible.

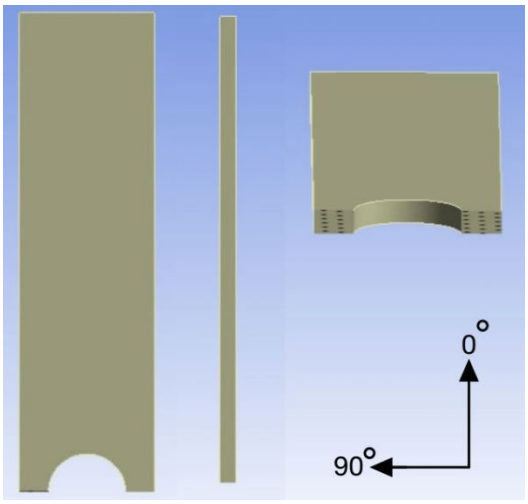

Figure 59. CFC section views and ply orientation reference: front view (left), side view (middle), and top-down view (right)

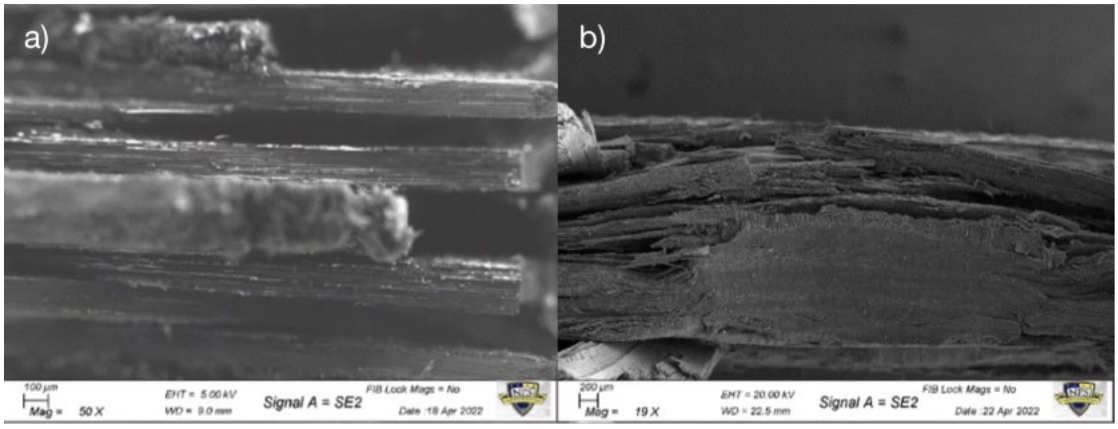

Figure 60. SEM top-down view of section A: a) Q1 sample (adjacent to the contact surface) and b) C1 sample (contact surface)

Upon further magnification, more failure mechanisms were observed. As shown in Figure 61a, fiber pull-out is clearly visible in the Q1 sample. Additionally, Figure 61 shows fiber/matrix debonding, as well as fiber failure in the Q1 and C1 samples.

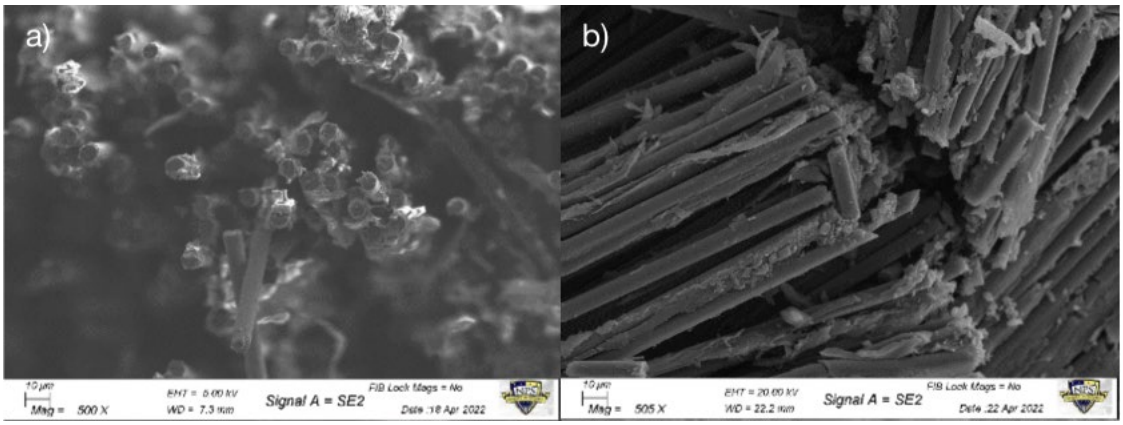

Figure 61. Further magnification of the sections shown in Figure 60: a) Q1 sample (adjacent to the contact surface) and b) C1 sample (contact surface)

Magnification to the individual fiber level revealed the brittleness of the carbon fiber filaments. As seen in Figure 62, clevage of the brittle carbon fiber reinforcements is observeable. Additionally, longitudinal lines along the fiber, from when the carbon fiber strands were initially drawn, can be seen. The textured surface on the carbon fiber filaments aids in matrix adhesion. Although it may appear in Figure 62b that the carbon fiber reinforcement failed under microbuckling, the fiber actually failed due to bending. As seen in Figure 60b, there was an out of plane force generated by the bolt that caused the 90º plies to bend outward.

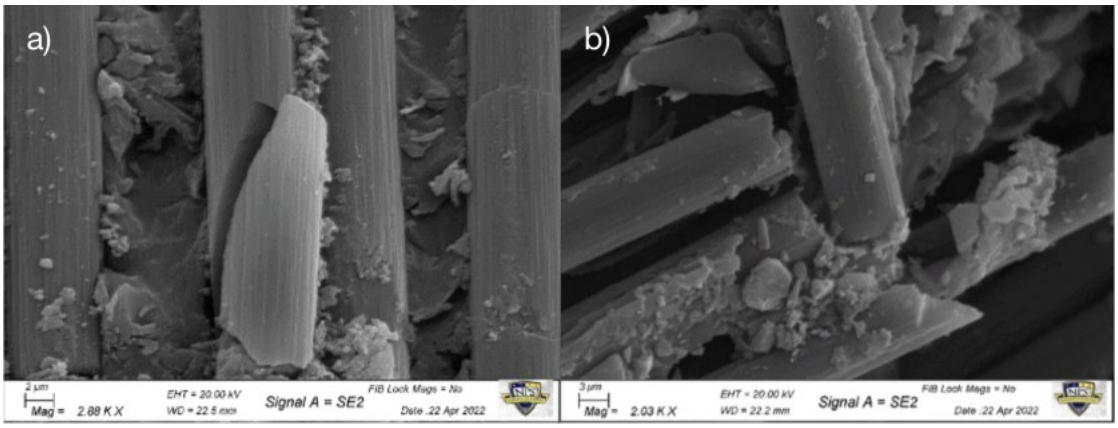

Figure 62. SEM top-down view of section A (contact surface) from C1 sample: a) brittle fracture and b) bending failure

Section A, from the Q1 and C1 samples, were then viewed in the SEM along their thickness (side view). The difference in ply layup between the QI and CP laminates is shown again in Figure 63. Figure 63 also shows delamination and matrix cracking in both composites.

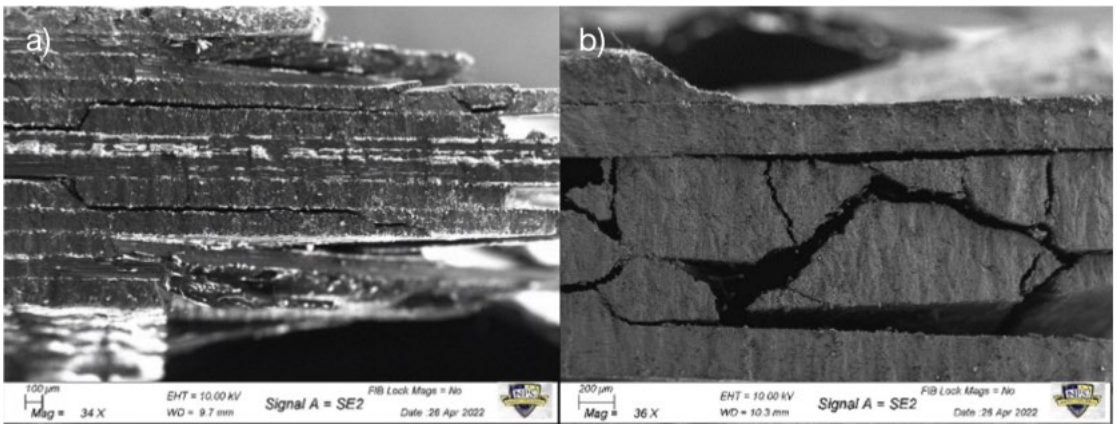

Figure 63. SEM side view of section A: a) Q1 sample and b) C1 sample

Section B, from the Q1 sample, was place in a cold mold and viewed under the optical microscope. In a view similar to Figure 63a, the optical microscope provides a somewhat different perspective of the fracture surface. As shown in Figure 64a, and similar to Figure 63a, delamination and matrix cracking is visible. However, unlike the SEM image, fiber failure is clearly observable. The lightest plies in the images are associated with the 0º carbon fiber filaments. For example, the 0º plies are located in the middle of Figure 64b. Figure 64b is provided so the reader may compare fractured and unfractured surfaces.

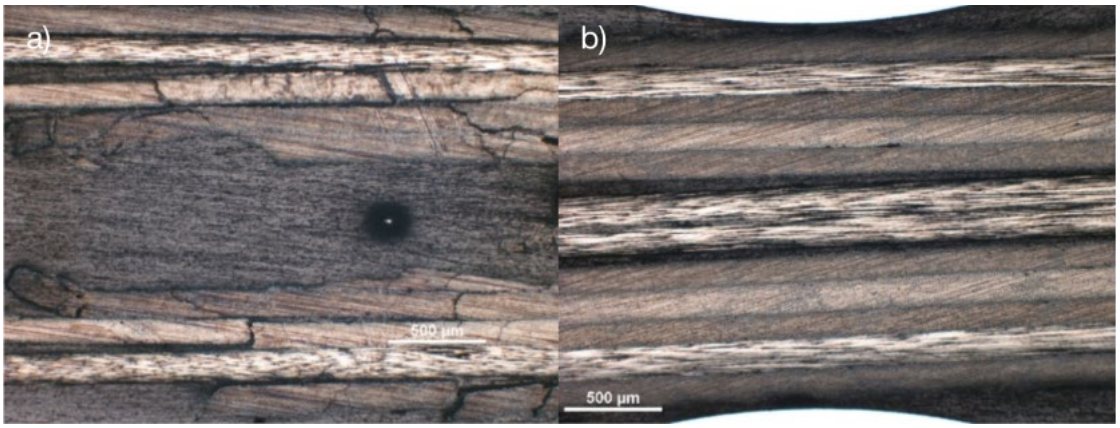

Figure 64. Optical microscope side view of section B from Q1 sample: a) fractured surface and b) unfractured surface

Unfortunatley, the C1 sample was not viewed under the optical microscope. Upon sectioning, in preparation for the cold mold, buckling delamination near the fracture surface resulted in the seperation of most plies. However, because the sample could not be viewed under the optical microscope, section A, from the C1 sample, was further examined in the SEM. The buckling delamination provided an opportunity to view the inner plies of the laminate without disturbing the original fractured surface. As shown in Figure 65a, the compressive stress of the bolt resulted in delamination and matrix cracking. In addition, as shown in Figure 65b, further magnification revealed fiber/matrix debonding, as well as numerous accounts of microbuckling.

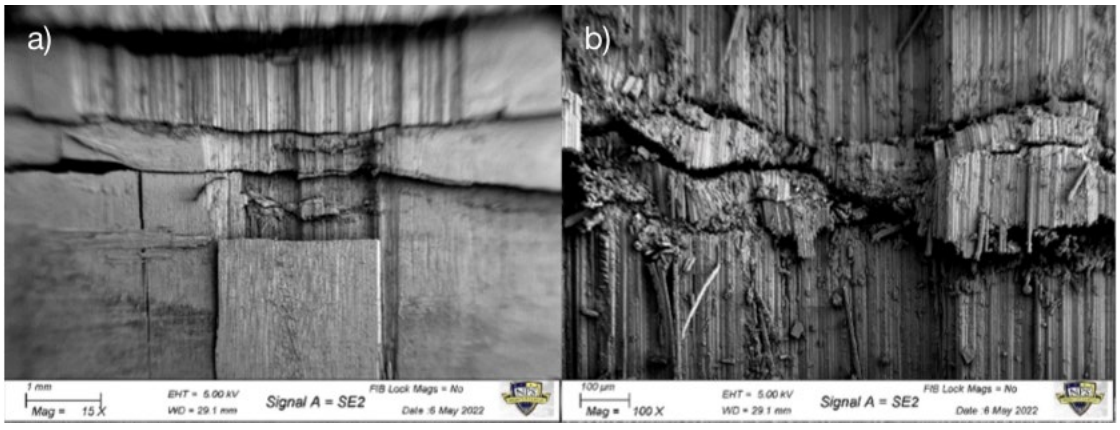

Figure 65. SEM front view of section A (above contact surface) from C1 sample: a) lower magnification and b) higher magnification

THIS PAGE INTENTIONALLY LEFT BLANK

V. CONCLUSION AND RECOMMENDATIONS

A. CONCLUSION

The objective of this research was twofold, progress toward a unified failure criteria and accurately predict the failure of bolt fastened brittle materials. In a sense, both objectives were accomplished. Although Kwon's recently proposed unified failure criteria was unable to provide sufficiently accurate failure predictions for bolt fastened PMMA, new discoveries were made which will hopefully aid in the refinement of the proposed failure criteria. The results strongly suggests that, for a brittle isotropic material, the location of failure initiation and the direction of initial crack propagation coincides with the maximum principal stress and the plane perpendicular to the maximum principal stress vector. Therefore, the failure location and direction can be predicted using an FEA model; however, as of now, the failure stress cannot be accurately determined.

Unfortunately, bolt fastened CFC failure predictions were unable to be made using a macromechanical approach and Kwon's failure criteria. As defined by Kwon's first criterion, the failure stress should exceed the failure strength of the material, which is obtained from a standard tensile test [6]. However, stress magnitudes obtained from all models were much lower than the tensile strength of the material. Therefore, due to an inability to identify an appropriate failure stress, or an exact failure location on the CFCs, predictions using Kwon's currently prescribed failure criteria were unachievable.

Although failure predictions were unable to be made for bolt fastened CFCs using the currently proposed failure criteria, the two models, which were produced for the analysis, revealed a vast difference in the modeling techniques. The ACP models provide much higher stress values compared to the homogeneous models. Unlike the homogeneous models, the ACP models account for variations in ply orientation, and therefore produced results that more accurately depict the load distribution in the laminate.

Bolt fastened CFC experimental test results revealed variation in the mechanical properties of the QI and CP CFCs. Due to the differences in ply orientation, more carbon

fiber filaments in the QI laminate were able to bear more of the load induced by the bolt in both QI parts. Therefore, the QI laminate was approximately 15% to 25% stronger than the CP laminate under similar loading conditions. Although the CP laminate was not as strong, the parts fabricated from the laminate did not succumb to net-tension or catastrophic failure throughout any test.

A fractographic analysis revealed many of the subcritical failure mechanisms associated with CFCs. Fiber failure, fiber/matrix debonding, matrix cracking, and delamination failure mechanisms were observed in both laminates. Fiber pull-out was only observed in the Q1 sample, which failed in a net-tension failure mode. Buckling delamination was clearly visible in the C1 sample. Additionally, the buckling delamination allowed access to the inner plies without having to disturb the fracture surface. Microbuckling, matrix cracking, fiber failure, fiber/matrix debonding, and delamination were all observable in the inner plies of the C1 sample.

In closing, although this study does not optimally validate Kwon's current failure criteria, it does provide newfound information for homogeneous isotropic and heterogeneous anisotropic brittle materials. Ideally, this research will aid in follow on research that will bring the field of fracture mechanics one step closer to a unified failure criteria for brittle and quasi-brittle materials.

B. RECOMMENDATIONS

First, prior studies conducted using Kwon's proposed failure criteria should be reassessed to determine if there is validity to the new findings. Should the studies agree, attempts should be made to refine the criteria. Ideally, a commonality in the gradients of all studies will be identified. Lastly, for use in a macromechanical approach, further testing should be conducted to identify the appropriate failure stress. As previously mentioned, the failure stress may be associated with one of the many CFC subcritical failure mechanisms.

LIST OF REFERENCES

[1] T. L. Anderson, *Fracture Mechanics*. Boca Raton, FL, USA: CRC Press, 2017.

[2] W. D. Callister and D. G. Rethwisch, *Materials Science and Engineering: An Introduction*, 9th ed. Hoboken, NJ, USA: Wiley, 2014.

[3] R. M. Jones, *Mechanics of Composite Materials*, 2nd ed. New York, NY, USA: Taylor & Francis Group, 1999.

[4] R. G. Budynas and J. K. Nisbett, *Shigley's Mechanical Engineering Design*, 11th ed. New York, NY, USA: McGraw-Hill Education, 2020.

[5] Y. W. Kwon, "Revisiting failure of brittle materials," *Journal of Pressure Vessel Technology*, vol. 143, no. 6, Dec. 2021.

[6] Y. W. Kwon, C. Diaz-Colon, and S. Defisher, "Failure criteria for brittle notched specimens," *Journal of Pressure Vessel Technology*, vol. 144, no. 5, Oct. 2022.

[7] A. Galinska, "Mechanical joining of fibre reinforced polymer composites to metals-A review. Part I: bolt joining," *Polymers*, vol. 12, Sep. 2020.

[8] M. A. McCarthy, V. P. Lawlor, W. F. Stanley, and C. T. McCarthy, "Bolt-hole clearance effects and strength criteria in single-bolt, single-lap, composite bolted joints," *Composites Science and Technology*, vol. 62, pp. 1415-1431, May 2002.

[9] K. Min, M. Silberstein, and N.R. Aluru, "Crosslinking PMMA: Molecular dynamics investigation of the shear response," *Journal of Polymer Science, Part B: Polymer Physics*, vol. 52, pp. 444-449, Dec. 2013.

[10] M. R. Ayatollahi, M. R. M. Aliha, and M. M. Hassani, "Mixed mode brittle fracture in PMMA – An experimental study using SCB specimens," *Materials Science & Engineering A*, vol. 417, pp. 348-356, Nov. 2005.

[11] DragonPlate, "What is Carbon Fiber?" Accessed May 27, 2022 [Online]. Available: https://dragonplate.com/

[12] SMI Composites, "Carbon Fiber Cost: Factors That Influence The Most." Accessed May 27, 2022 [Online]. Available: https://smicomposites.com/carbon-fiber-cost-factors-that-influence-the-most/

[13] A. C. Ugural and S. K. Fenster, *Advanced Mechanics of Materials and Applied Elasticity*, 5th ed. Upper Saddle River, NJ, USA: Pearson Education, Inc., 2012.

[14] Chemeurope.com, “Fracture Mechanics.” Accessed Oct. 15, 2022 [Online]. Available: https://www.chemeurope.com/en/encyclopedia/Fracture_mechanics.html

[15] J. J. Mecholsky Jr., “Fracture mechanics principles,” *Dental Materials*, vol. 11, no. 2, pp. 111-112, Mar. 1995.

[16] D. Taylor, *The Theory of Critical Distances: A New Perspective in Fracture Mechanics*. London, UK: Elsevier, 2007.

[17] P. P. Camanho, G. H. Ercin, G. Catalanotti, S. Mahdi, and P. Linde, “A finite fracture mechanics model for the prediction of the open-hole strength of composite laminates,” *Composites: Part A*, vol. 43, pp. 1219-1225, Mar. 2012.

[18] D. Taylor, P. Cornetti, and N. Pugno, “The fracture mechanics of finite crack extension,” *Engineering Fracture Mechanics*, vol. 72, pp. 1021-1038, Jul. 2004.

[19] DragonPlate, “0/90 Degree Carbon Fiber Uni Sheet ~ 1/16” x 12” x 12”.” Accessed Oct. 27, 2022 [Online]. Available: https://dragonplate.com/0_90-Degree-Carbon-Fiber-Uni-Sheet-1_16-x-12-x-12

[20] DragonPlate, “Quasi-isotropic Carbon Fiber Uni Sheet ~ 1/16” x 12” x 12”.” Accessed Oct. 27, 2022 [Online]. Available: https://dragonplate.com/Quasi-isotropic-Carbon-Fiber-Uni-Sheet-1_16-x-12-x-12

[21] G. Kelly and S. Hallstrom, “Bearing strength of carbon fibre/epoxy laminates: effects of bolt-hole clearance,” *Composites Part B: Engineering*, vol. 35, pp. 331-343, Nov. 2003.

[22] Instron, “5980 Series Universal Testing System | Up to 600 kN Force Capacity.” Accessed Oct 29, 2022 [Online]. Available: https://www.instron.com/en/products/testing-systems/universal-testing-systems/high-force-universal-testing-systems/5989-floor-model

[23] J. Schon, “Coefficient of friction and wear of a carbon fiber epoxy matrix composite,” *Wear*, vol. 257, no. 3-4, pp. 395-407, Aug. 2004.

[24] S. Matsunaga, T. Matsubara, W. Wang, and Y. Takao, “Effects of Reciprocation Number on the Friction Behaviors of Carbon/Epoxy for Various Fiber Orientations and High Contact Pressures,” in *Proceedings of the ICCM-13*, Beijing, China, 2001, p. ID 1446.

INITIAL DISTRIBUTION LIST

1. Defense Technical Information Center
   Ft. Belvoir, Virginia

2. Dudley Knox Library
   Naval Postgraduate School
   Monterey, California